

Electronic, vibrational, and electron-phonon coupling properties in SnSe₂ and SnS₂ under pressure

Gyanu Prasad Kafle,¹ Christoph Heil,² Hari Paudyal,¹ and Elena R. Margine^{1,*}

¹*Department of Physics, Applied Physics, and Astronomy,
Binghamton University-SUNY, Binghamton, New York 13902, USA*

²*Institute of Theoretical and Computational Physics,
Graz University of Technology, NAWI Graz, 8010 Graz, Austria*

(Dated: October 23, 2020)

The tin-selenide and tin-sulfide classes of materials undergo multiple structural transitions under high pressure leading to periodic lattice distortions, superconductivity, and topologically non-trivial phases, yet a number of controversies exist regarding the structural transformations in these systems. We perform first-principles calculations within the framework of density functional theory and a careful comparison of our results with available experiments on SnSe₂ reveals that the apparent contradictions among high-pressure results can be attributed to differences in experimental conditions. We further demonstrate that under hydrostatic pressure a $\sqrt{3} \times \sqrt{3} \times 1$ superstructure can be stabilized above 20 GPa in SnS₂ via a periodic lattice distortion as found recently in the case of SnSe₂, and that this pressure-induced phase transition is due to the combined effect of Fermi surface nesting and electron-phonon coupling at a momentum wave vector $\mathbf{q} = (1/3, 1/3, 0)$. In addition, we investigate the contribution of nonadiabatic corrections on the calculated phonon frequencies, and show that the quantitative agreement between theory and experiment for the high-energy A_{1g} phonon mode is improved when these effects are taken into account. Finally, we examine the nature of the superconducting state recently observed in SnSe₂ under nonhydrostatic pressure and predict the emergence of superconductivity with a comparable critical temperature in SnS₂ under similar experimental conditions. Interestingly, in the periodic lattice distorted phases, the critical temperature is found to be reduced by an order of magnitude due to the restructuring of the Fermi surface.

I. INTRODUCTION

Tin-based binary compounds, Sn_xSe_y and Sn_xS_y, have emerged as promising candidates for electronic, optoelectronic, photovoltaic, and thermoelectric applications¹⁻⁸ as well as platforms for exploring exotic states of matter⁹⁻¹³. Similar to other layered metal chalcogenide materials¹⁴⁻²¹, it has been found that under increased pressure and/or temperature these compounds undergo substantial changes in their structural and electronic properties, special interest being paid to those materials that can host charge density wave (CDW), superconducting, or topologically non-trivial phases^{9-13,19,22-28}.

In the dichalcogenide systems, pressure-induced structural phase transitions have been reported for both SnSe₂ and SnS₂. For example, two theoretical studies have predicted that SnSe₂ becomes thermodynamically unstable above 18-20 GPa and then decomposes into Sn₃Se₄ (space group $I\bar{4}3d$) and Se^{10,22}. A similar decomposition has been theoretically shown to take place in the sister compound SnS₂, which remains thermodynamically stable up to approximately 28 GPa²³. We would like to note in passing that both 3:4 compounds have been recently predicted to be superconducting with T_c values of 3.3-4.7 K at 10 GPa^{10,11}, and 21.9 K at 30 GPa²³, respectively. Although the formation of Sn₃Se₄ and Sn₃S₄ has been reported in experiments^{10,29}, the presence of a superconducting state in these materials still awaits experimental confirmation.

While SnSe₂ is no longer on the convex hull tie-line at

higher pressures and also becomes dynamically unstable, we have shown in a previous study¹⁹ that it can be stabilized in a $\sqrt{3} \times \sqrt{3} \times 1$ supercell through a periodic lattice distortion (PLD) and that it can, in fact, be realized in experiments. In particular, under applying pressure, SnSe₂ becomes metallic in the 8-13 GPa range, with a typical metallic behavior above 17 GPa, and transitions to the PLD phase at around 17 GPa. The agreement between theory and experiment was very good, and the experimentally observed phase transition has been successfully ascribed to a combined effect of electron-phonon (e-ph) coupling and Fermi surface (FS) nesting. This is in contrast to transitional metal dichalcogenides (TMDs), where FS nesting is found to only play a minor role in creating the CDW instability^{20,30-33}. Interestingly, in another recent high-pressure experimental study²⁸, neither the proposed theoretical decomposition^{10,22} nor the transformation to the PLD phase¹⁹ were detected up to 46 GPa. Instead, electrical resistance measurements in compressed SnSe₂ showed an insulator-to-metallic transition above 15.2 GPa and the appearance of a superconducting state around 18.6 GPa.

In the present study, we first address the apparent contradiction among high-pressure experimental results in SnSe₂ above 20 GPa. Next, we explore whether a $\sqrt{3} \times \sqrt{3} \times 1$ superstructure can also be stabilized in SnS₂ via a PLD by providing a detailed comparison of the electronic, vibrational, and e-ph properties of the two compounds. We expand on our previous work¹⁹ to improve the quantitative agreement between theory and experi-

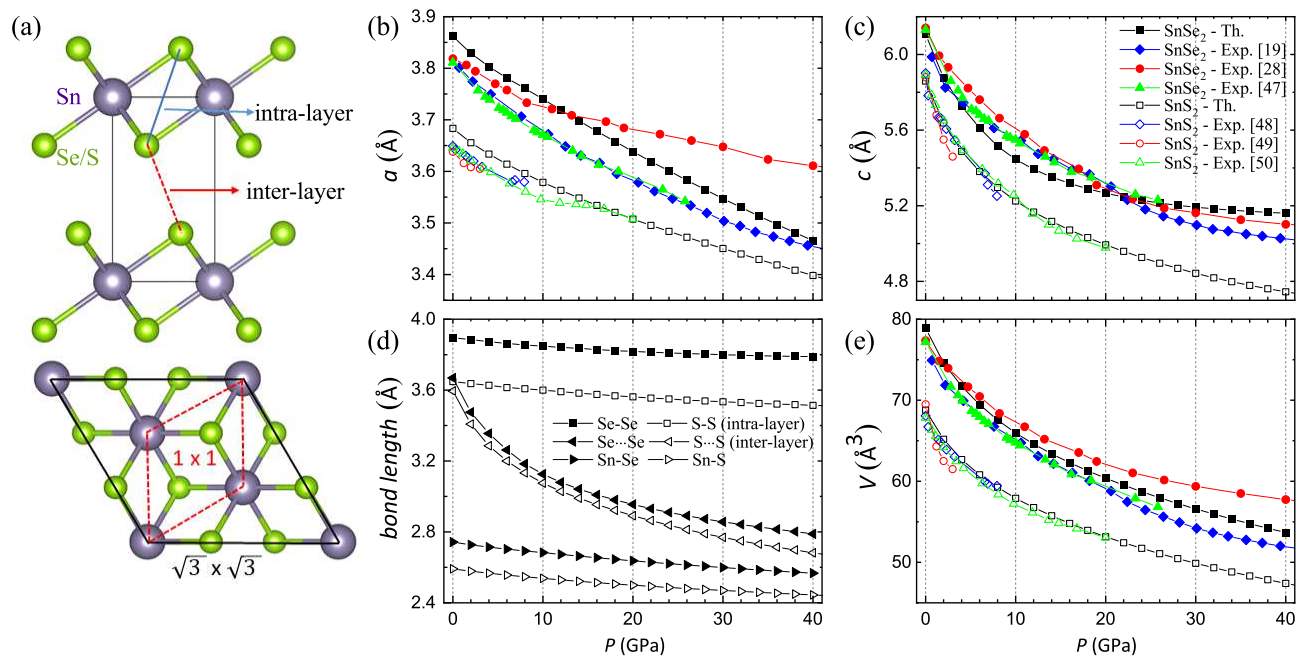


FIG. 1: (a) Crystal structures showing the intra-layer (Se-Se/S-S) and inter-layer (Se \cdots Se/S \cdots S) distances (top figure) and 1×1 and $\sqrt{3} \times \sqrt{3}$ unit cells (bottom figure). Pressure dependence of (b), (c) the lattice parameters a and c , (d) the average bond lengths, and (e) the volume per one formula unit for SnSe₂ and SnS₂. Theoretical results are shown as black symbols and are compared with available experimental data^{19,28,47–50}. Data for SnSe₂ and SnS₂ are presented with solid and open symbols.

ment with respect to the pressure dependence of the A_{1g} phonon mode. In particular, we investigate the effect of LO-TO splitting and nonadiabatic corrections on the calculated phonon frequencies. Finally, we investigate the origin of the superconducting state recently observed in SnSe₂ under nonhydrostatic pressure, and shed light on the superconducting properties of SnS₂ and the PLD phases of the two systems at higher pressures.

II. METHODS

First-principles calculations were performed within the density functional theory (DFT) using the Quantum ESPRESSO (QE)³⁴ code. We employed optimized norm-conserving Vanderbilt (ONCV) pseudopotentials³⁵ with the Perdew-Burke-Ernzerhof (PBE) exchange-correlation functional in the generalized gradient approximation³⁶, where the Sn $4d^{10}5s^25p^2$, Se $4s^24p^4$, and S $3s^23p^4$ orbitals were included as valence electrons. To properly treat the long-range dispersive interactions, we used the non-local van der Waals (vdW) density functional optB86b-vdW^{37,38}. A plane wave kinetic-energy cutoff value of 60 Ry, a Marzari-Vanderbilt cold smearing³⁹ value of 0.01 Ry, and a Γ -centered $24 \times 24 \times 16$ Monkhorst-Pack⁴⁰ \mathbf{k} -mesh for the three-atom unit cell and $12 \times 12 \times 16$ \mathbf{k} -mesh for the nine-atom $\sqrt{3} \times \sqrt{3} \times 1$ supercell were used for the Brillouin-zone (BZ) integration. The atomic positions and lattice parameters were optimized until the self-consistent energy was converged within 2.7×10^{-5} eV and

the maximum Hellmann-Feynman force on each atom was less than 0.005 eV/Å. The dynamical matrices and the linear variation of the self-consistent potential were calculated within density-functional perturbation theory (DFPT)⁴¹ on the irreducible set of a regular $6 \times 6 \times 4$ \mathbf{q} -mesh for the three-atom unit cell and $3 \times 3 \times 4$ \mathbf{q} -mesh for the nine-atom $\sqrt{3} \times \sqrt{3} \times 1$ supercell.

The EPW code^{42,43} was used to compute e-ph interactions and related properties. The electronic wavefunctions required for the Wannier-Fourier interpolation^{44,45} were calculated on a uniform Γ -centered $12 \times 12 \times 4$ \mathbf{k} -grid for the three-atom unit cell. Ten maximally localized Wannier functions (one s and three p orbitals for each Sn atom and three p orbitals for each chalcogen atom) were used to describe the electronic structure near the Fermi level (E_F). A uniform $300 \times 300 \times 200$ \mathbf{k} -mesh was used to evaluate the adiabatic phonon self-energy and static bare susceptibility, while 2 million random \mathbf{k} points were used to estimate the phonon spectral function in the nonadiabatic regime. Both sets of calculations were performed along a high-symmetry path in \mathbf{q} -space with smearings of 25 meV (electrons) and 0.05 meV (phonons). Uniform $120 \times 120 \times 40$ \mathbf{k} -point and $60 \times 60 \times 20$ \mathbf{q} -point grids were used for the superconductivity calculations in the three-atom unit cell (the in-plane meshes were reduced by a factor of three in the nine-atom supercell). The Matsubara frequency cutoff was set to 0.4 eV and the Dirac deltas were replaced by Lorentzians of width 25 meV (electrons) and 0.1 meV (phonons) when solving the isotropic Migdal-Eliashberg equations.

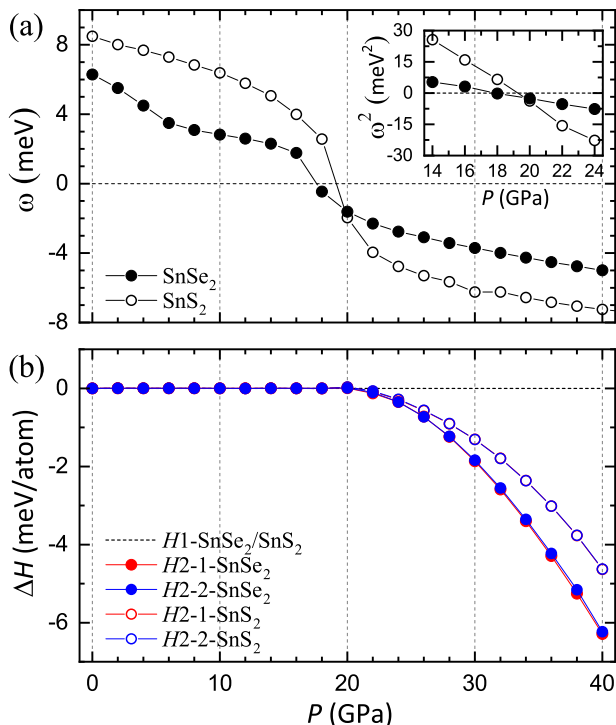


FIG. 2: (a) Calculated softening of the lowest-energy (degenerate) phonon modes in the $\sqrt{3} \times \sqrt{3} \times 1$ $H1$ superlattice for SnSe_2 and SnS_2 , where imaginary phonon frequencies are shown as negative, illustrating the pressure-induced destabilization of the $H1$ phase. The inset shows the squared frequency of the modes. (b) Enthalpy difference for the considered $H2$ structures as function of pressure for SnSe_2 and SnS_2 , where the $H1$ phase was chosen as a reference.

III. RESULTS

A. Crystal structure evolution under pressure

At ambient conditions, bulk SnSe_2 and SnS_2 crystalize in the hexagonal, close-packed CdI_2 -type structure with space group $P\bar{3}m1$ (No. 164)^{19,46}. The unit cell contains three atoms, where every Sn atom occupies the center of an octahedron formed by six chalcogen atoms (Se or S) [see Fig. 1(a)]. We refer to this high-symmetry structure as the $H1$ phase. Fig. 1(b)-(e) presents the optimized structural parameters as a function of pressure, together with available experimental data for comparison^{19,28,47-50}.

As pointed out in previous studies⁴⁸⁻⁵⁰, the contraction of the unit cell under compression is highly anisotropic. According to our theoretical results for hydrostatic pressure, the lattice parameter along the a axis decreases almost linearly with increasing pressure, while that along the c axis shrinks quickly before beginning a slower descent. This anisotropic compression can be related to the rapid decrease in the inter-layer $\text{Se}\cdots\text{Se}/\text{S}\cdots\text{S}$ distance (i.e., the distance between the chalcogen atoms in adjacent layers) versus the intra-layer $\text{Se-Se}/\text{S-S}$ and

$\text{Sn-Se}/\text{Sn-S}$ distances due to the weaker vdW inter-layer interaction relative to the stronger covalent intra-layer bonding.

Up to 10 GPa, there are no appreciable differences seen in the compressibility rates in the two systems. For instance, the lengths of the a and c axes at 10 GPa are reduced by about 3% and 11% with respect to their zero-pressure values in both cases. As the pressure increases, the compressibility rate along the a axis becomes slightly smaller in SnS_2 than in SnSe_2 , following the expected trend that a more covalent intra-layer bond is less compressible⁴⁷ [see Supplemental Fig. S1⁵¹]. The compressibility rate along the c axis, on the other hand, displays the opposite behavior. This can be empirically understood from the relatively more localized nature of the $3p$ orbitals of S^{-2} compared to the $4p$ orbitals of Se^{-2} , which gives rise to a weaker interaction across the vdW gap in SnS_2 and thus increased compressibility.

The present theoretical results for the pressure dependence of the cell parameters are in very good agreement with all experimental data in the low pressure region between 0 and 10 GPa [see Fig. 1]. Beyond this point, the pressure transmitting medium used in various experiments can cause considerable differences between the compressed lattice parameters. The largest deviation is observed for the compression of the a axis in SnSe_2 beyond 10 GPa in Ref. [28] and is attributed to nonhydrostatic pressure conditions in the experimental setup. A similar, but smaller effect, was also found in SnS_2 ^{48,50}.

We next discuss the thermodynamic and dynamic stability of SnSe_2 and SnS_2 under compression. With respect to the full phase diagram, our calculations agree well with the findings reported in literature, namely that SnSe_2 and SnS_2 lie above the convex hull tie-line for pressures above approximately 20 and 40 GPa, respectively [see Supplemental Fig. S2⁵¹]. The occurrence of a lattice instability is established by calculating the full phonon dispersion relations in the harmonic approximation in the three-atom $H1$ unit cell. As shown in Supplemental Fig. S3⁵¹, the lowest-energy vibrational mode has an imaginary frequency at the K point of the BZ at 20 GPa, indicating that the two systems have become dynamically unstable. Based on the above results, it would be expected that the systems will either decompose into more stable products or undergo a crystal transformation into a nearby minima in the configuration space by following the eigenvector of a soft phonon mode.

The successful synthesis of Sn_3Se_4 in laser-heated diamond anvil cells¹⁰ points towards the first scenario, but no traces of the Sn_3Se_4 phase were detected in the high-pressure synchrotron x-ray diffraction (XRD) patterns measured at room temperature in two other recent studies^{19,28}. This implies that a relatively large activation barrier needs to be overcome for the system to decompose, requiring not only high pressures but also high temperatures.

Evidence for the second scenario has also been provided in our combined experimental and theoretical work

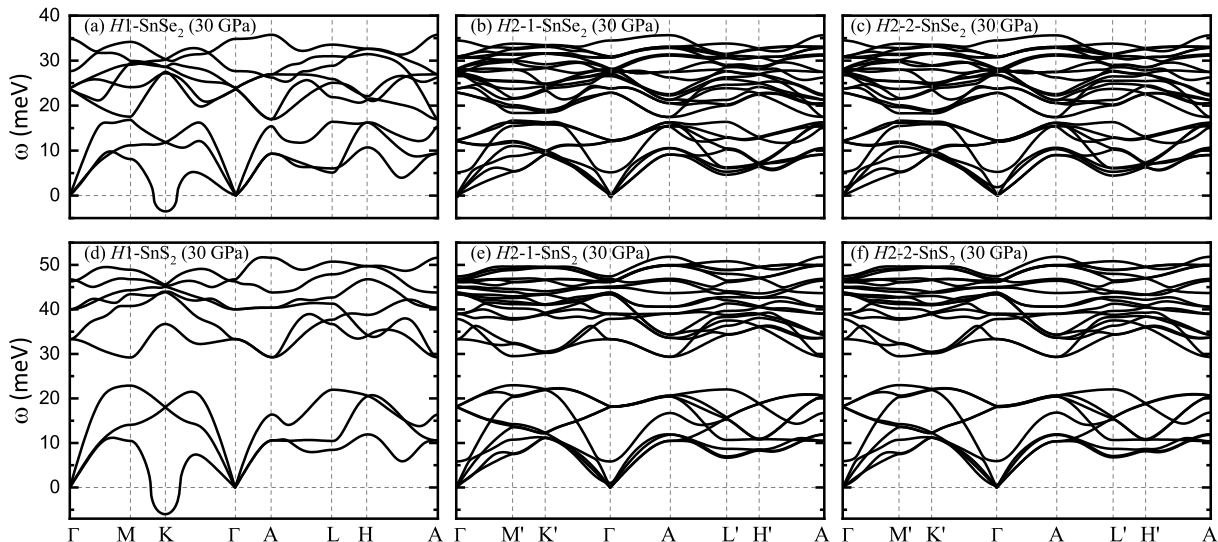


FIG. 3: Calculated phonon dispersion for the (a), (d) $H1$ structure in the $1 \times 1 \times 1$ unit cell and (b), (c), (e), (f) $H2$ structures in the $\sqrt{3} \times \sqrt{3} \times 1$ supercell of SnSe_2 (top row) and SnS_2 (bottom row) at 30 GPa. The $H2-1$ and $H2-2$ structures are derivatives of the undistorted $\sqrt{3} \times \sqrt{3} \times 1$ $H1$ structure created via a PLD.

on SnSe_2 ¹⁹. Namely, the formation of a $\sqrt{3} \times \sqrt{3} \times 1$ superlattice has been revealed through the sudden appearance of several reflections at $(1/3, 1/3, 0)$ in XRD patterns and of two new peaks in the Raman spectra above 17 GPa. In addition, it has been shown that energetically more stable structures with lower symmetry can be constructed as detailed below. Here we will refer to the derivatives of the undistorted $\sqrt{3} \times \sqrt{3} \times 1$ $H1$ structure created via a PLD as $H2$. The fact that SnSe_2 has not been synthesized in the $H2$ structure in the study by Zhou *et al.*²⁸ suggests that the formation of this metastable phase is strongly dependent on the experimental conditions. While the NaCl powder used in our high-pressure XRD experiments ensured a quasi-hydrostatic pressure environment below 40 GPa¹⁹, the silicone oil used as a pressure transmitting medium by Zhou *et al.* produced nonhydrostatic pressures above 13.2 GPa²⁸. A similar situation has been observed for TMDs, where different pressure conditions give rise to variations in the structural and electronic properties.^{52,53} For instance, in the case of WS_2 , the transition from the $2H_c$ to $2H_a$ phase occurred under nonhydrostatic, but not under hydrostatic pressure⁵³.

We now focus our attention on understanding whether a $\sqrt{3} \times \sqrt{3} \times 1$ superstructure can also be stabilized in SnS_2 via a PLD. Since the K point of the $1 \times 1 \times 1$ unit cell folds onto the Γ point in the $\sqrt{3} \times \sqrt{3} \times 1$ supercell, dynamical stability calculations can be performed by determining the phonon frequencies at the Γ point of the nine-atom $H1$ structure. As pressure is increased, the two nearly degenerate lowest-energy phonon modes with A_{2g} and A_{2u} symmetry soften and become imaginary as shown in Fig. 2(a). The linear evolution of ω^2 with pressure [Fig. 2(a) inset] is a characteristic feature of a soft-mode phase transition^{54,55}, enabling us to estimate

the critical transition pressure when ω^2 goes to zero. In this case, we obtain 18 GPa for SnSe_2 and 19 GPa for SnS_2 , respectively.

To construct the energetically preferred structural derivatives of the original $H1$ phase, we follow the same strategy employed in our previous work on SnSe_2 ¹⁹. We displace the atomic coordinates according to the eigenvectors of A_{2g} ($H2-1$ phase) and A_{2u} ($H2-2$ phase) modes as well as a linear combination of the two eigenvectors ($H2-3$ phase) to better explore the adiabatic potential energy surface. As for SnSe_2 , the resulting distorted structures for the $\sqrt{3} \times \sqrt{3} \times 1$ supercell are fully relaxed and found to converge to three distinct configurations based on the structure analysis performed with the MAISE package⁵⁶. The lattice parameters, space groups, and Wyckoff positions of $H2$ structures at 30 GPa are given in Table. S1 and the crystal structures are shown in Fig. S4⁵¹. Since $H2-3$ is an intermediate phase along the pathway that transforms $H2-1$ into $H2-2$, we will only concentrate on the $H2-1$ and $H2-2$ structures in our further discussion.

As can be appreciated from the pressure dependence plots of the relative enthalpy in Fig. 2(b), the $H2$ phases are energetically more favorable above 18 and 20 GPa for SnSe_2 and SnS_2 , respectively. This is in good agreement with our phonon calculations at 30 GPa, showing no imaginary frequencies and demonstrating the dynamical stability of the predicted $H2$ phases [Fig. 3]. We find the $H2$ derivatives to be virtually degenerate in enthalpy and no distinguishable differences between their phonon spectra. A comparison of the radial distribution functions (RDFs) shown in Fig. 4 along with an estimate of the similarity factor (defined as the RDF dot product between two structures) provide further evidence that the $H2-1$ and $H2-2$ configurations are indeed distinct

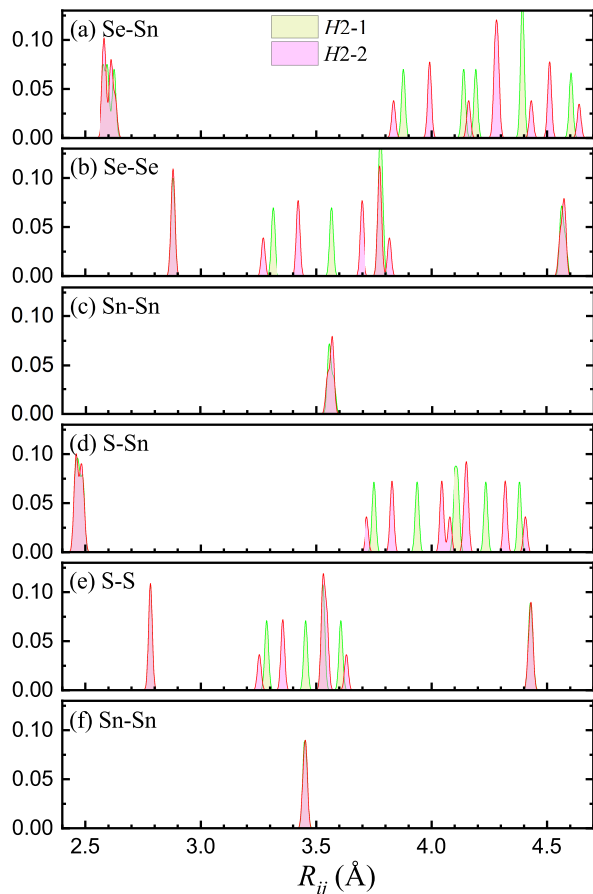


FIG. 4: Calculated radial distribution function of the $H2$ structures for (a)-(c) SnSe_2 and (d)-(f) SnS_2 at 30 GPa with MAISE⁵⁶.

despite having similar enthalpies. In this case, using a Gaussian spread of 0.008⁵⁶, we find a similarity factor of 0.5358 and 0.6102 between the $H2-1$ and $H2-2$ structures for the SnSe_2 and SnS_2 systems, respectively. Noticeably, the main difference in the RDFs comes from the second-nearest neighbor, explaining the similar covalent network and, therefore, the very similar vibrational and low-energy electron properties of the $H2$ derivatives. Based on the RDF analysis, we can establish that the distorted configurations are nearby local minima, a situation encountered in other systems⁵⁷.

B. Electronic properties

In this section we systematically analyze the band structure of SnSe_2 and SnS_2 under hydrostatic and non-hydrostatic pressure. At zero pressure, both systems are found to be semiconducting with an indirect band gap of 0.62 eV in SnSe_2 and 1.35 eV in SnS_2 , respectively. As for bulk TMDs consisting of the same transition metal, the compound with the most electronegative chalcogen has the largest band gap⁵⁸⁻⁶¹. While this is the correct

trend, we need to keep in mind in our following discussion that the size of the band gaps are underestimated relative to those extracted from experiments⁶²⁻⁶⁶ or calculated with the GW approximation or the HSE06 hybrid functional^{65,67}.

Figure 5 shows the calculated hydrostatic band structures for the $H1$ phase in the three-atom unit cell at 0, 6, and 20 GPa; band structures at other pressures are given in Supplemental Fig. S5⁵¹. The bottom of the conduction band displays a mixture of Sn s with chalcogen (Se or S) p_{xy} orbitals along the in-plane directions and with chalcogen p_z orbitals along the out-of-plane directions. The top of the valence band, on the other hand, consists almost entirely of chalcogen p_z orbitals. Under compression, the orbital character of the bands remains largely unaffected, but the bandwidths expand as indicated by the increase in the slope of the dispersion curves. Near the Fermi level, the most significant change takes place in the lowest conduction band level along the $\Gamma - K$ segment. Due to a greater overlap between the chalcogen p_{xy} and Sn s orbitals, the band energy at the K point decreases, eventually dropping below the valence band maximum and closing the band gap. As a result, a pressure-induced semiconductor-to-metal transition is estimated to occur at 6 and 20 GPa in SnSe_2 and SnS_2 , respectively.

The predicted metallization pressures are consistent with available theoretical results^{19,22,50}, but lower than the experimental values as anticipated from the underestimation of the band gaps in the PBE approximation. Additional changes in the metallization pressure are also expected under nonhydrostatic pressure conditions. DFT results show that a transition at a higher (lower) pressure is favored under in-plane (out-of-plane) uniaxial compressive strain [see Supplemental Fig. S6⁵¹]. This trend is in agreement with experimental resistivity measurements in SnSe_2 where a semiconductor-to-metal transition was observed between 8-13 GPa under quasi-hydrostatic pressure¹⁹ compared to a transition above 15.2 GPa under nonhydrostatic pressure²⁸. As can be seen in Fig. 1(b), the in-plane compression in the latter study is considerable smaller, thus pushing the metallization point to a higher pressure.

To get a better understanding of how the internal structural parameters of the layers, the inter-layer distance, and the choice of chalcogen atom affect the electronic transition, we calculate the electronic dispersions of (i) SnSe_2 structure at 0 GPa in which the Se atoms are substituted with S and the atomic coordinates are either kept unchanged (labeled as $\text{SnSe}_2\text{-str-S}$) or allowed to relax (labeled as $\text{SnSe}_2\text{-str-S-relaxed}$), and (ii) SnS_2 structure at 0 GPa in which the S atoms are substituted with Se and the atomic coordinates are either kept unchanged (labeled as $\text{SnS}_2\text{-str-Se}$) or allowed to relax (labeled as $\text{SnS}_2\text{-str-Se-relaxed}$).

As shown in Supplemental Fig. S7⁵¹, the effect of replacing Se with S is an up-shift of the lowest conduction band states and, consequently, a slight increase in the band gap from 0.62 to 0.75 eV. Allowing the atoms to

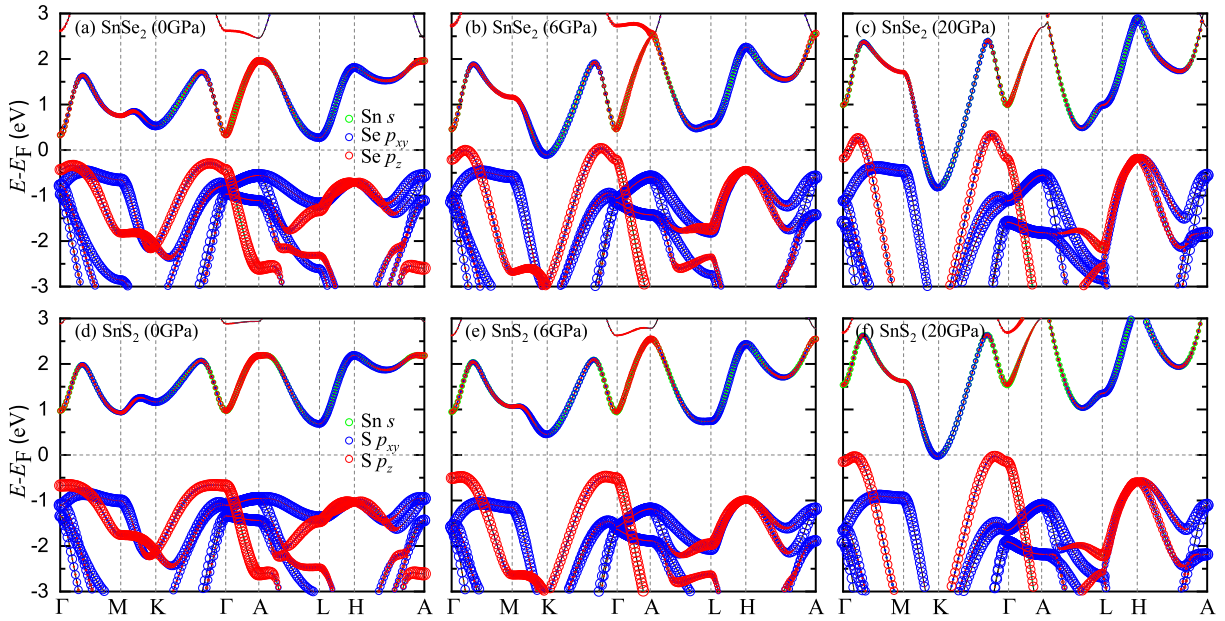


FIG. 5: Calculated band structure for the $H1$ structure in the $1 \times 1 \times 1$ unit cell of (a)-(c) SnSe_2 and (d)-(f) SnS_2 at 0, 6, and 20 GPa. The size of the symbols is proportional to the contribution of each orbital character.

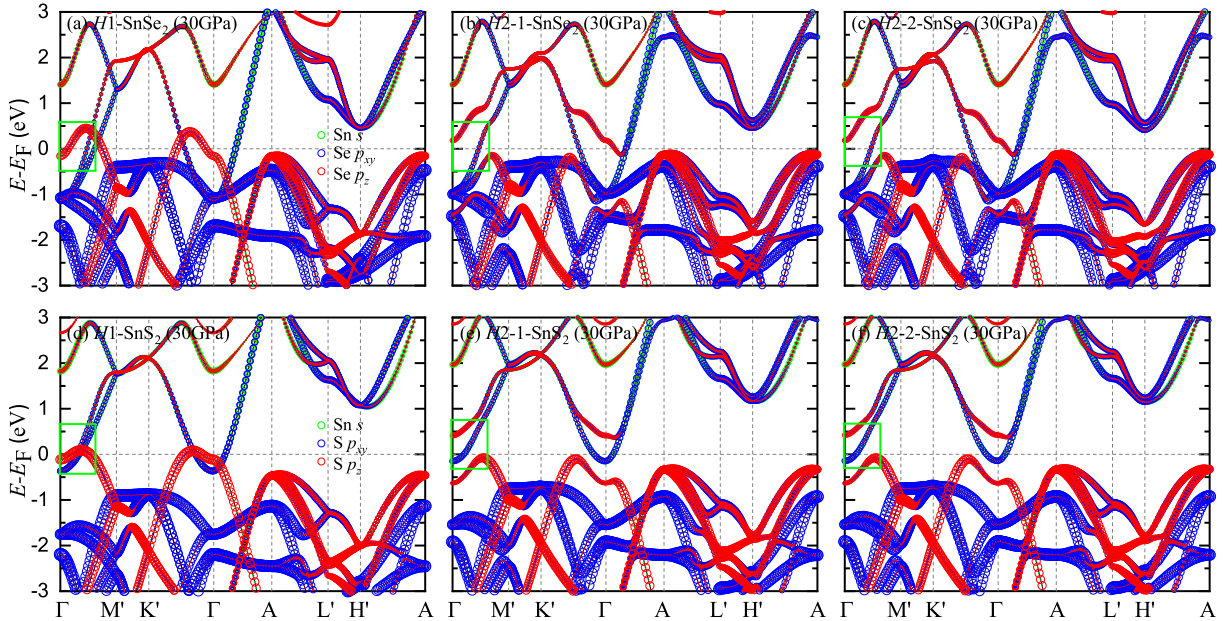


FIG. 6: Calculated band structure for the (a), (d) $H1$ and (b), (c), (e), (f) $H2$ structures in the $\sqrt{3} \times \sqrt{3} \times 1$ supercell of SnSe_2 (top row) and SnS_2 (bottom row) at 30 GPa. The $H2-1$ and $H2-2$ structures are derivatives of the undistorted $\sqrt{3} \times \sqrt{3} \times 1$ $H1$ structure created via a PLD. The area indicated by the green box in (a), (d) is to be compared to (b), (e) and (c), (f) where avoided crossing near the Fermi level can be observed in the $H2$ structures.

relax gives an additional up-shift of 0.15 eV since the intra-layer distance is reduced to almost the ideal value in SnS_2 . However this up-shift is still not large enough to reach the band gap value of SnS_2 . If, on the other hand, we use the SnS_2 structure with the Se pseudopotential, as in calculation (ii), we see an opposite trend since now the

lowest conduction band states move down in energy. The band gap reduces from 1.35 to 0.90 eV without atomic relaxation and further to 0.22 eV once the atoms are allowed to relax. The reduction by a factor of almost three of the band gap relative to the value in ideal SnSe_2 can be ascribed to the presence of slightly more charge in the

vdW gap as the inter-layer distance is compressed by almost 10%. Supplemental Figs. S8 and S9⁵¹ show total charge and charge redistribution plots for the configurations described above. Overall, the metallization process is driven by the cooperative effect of both chemical and structural factors.

We further study the evolution of the charge density with pressure. Similar to TMDs, we find that under compression more electronic charge moves away from the Sn atoms and accumulates along the intra-layer bonds formed by Sn with the chalcogen atoms and in the inter-layer region between the chalcogen atoms^{68–70} [Supplemental Figs. S10⁵¹]. This view is also supported by the increase in the in-plane average charge at the middle of the vdW gap under applied pressure [see Supplemental Figs. S11⁵¹ showing the in-plane average charge as a function of the perpendicular direction with respect to the layer]. This behavior is in contrast to intercalated carbon and boron layered compounds where, under applied pressure, the inter-layer charge from the intercalant atoms is forced out to the covalent sheets^{71–73}.

Finally, in Fig. 6 we compare the electronic structure of $H1$ and $H2$ phases in the $\sqrt{3} \times \sqrt{3} \times 1$ supercell for the two systems. As shown in our previous study on SnSe_2 ¹⁹, the main difference lies in the lifting of electronic degeneracy near the Fermi level along the $\Gamma - M$ and $K - \Gamma - A$ directions in the $H2$ structures. Compared to the parent $H1$ phase, there is an out-of-plane displacement of the Sn atoms resulting in a slight buckling of the Sn layers and a shift of the chalcogen atoms with respect to the center of the octahedron [see Supplemental Fig. S4⁵¹]. This modulation of atomic positions leads to the avoidance of crossings between the bands with mixed Sn s and chalcogen p_{xy} orbitals and the band with chalcogen p_z character. Similarly to the phonon spectra in Fig. 3, there are no noticeable differences between the band structure plots of the $H2$ derivatives.

C. Vibrational properties

In low-dimensional or layered systems, the appearance of a superlattice is often the signature of a CDW transition, as for example in TMDs^{31,32}. In these materials, it has been established that the wave vector dependence of the e-ph coupling is crucial in understanding the CDW formation, while the FS nesting has been found to only play a minor role^{20,30–33}. As presented in our previous study on SnSe_2 ¹⁹, the breaking of electronic degeneracies by a phonon-modulated lattice distortion, the reduction of the density of states (DOS) at the Fermi level, and the softening of a low-energy phonon are key signatures of a momentum-dependent e-ph coupling CDW instability. In this section, we want to investigate if the same reasoning is true for SnS_2 as well.

To address the microscopic mechanism responsible for the phase transition and the origin of phonon softening at K , we calculate the adiabatic phonon self-energy

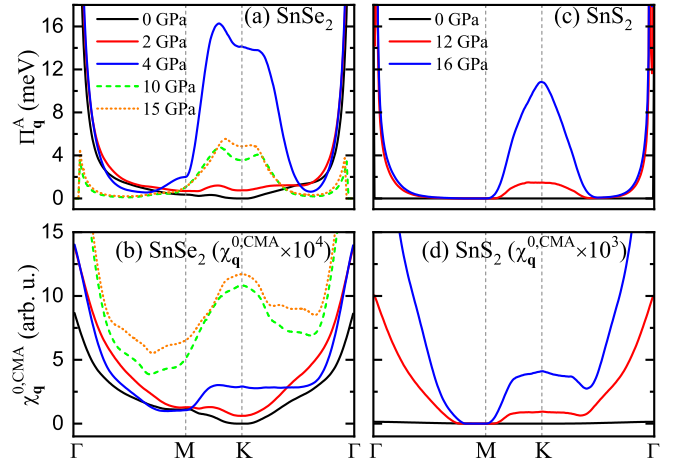


FIG. 7: The adiabatic phonon self-energy for the soft phonon mode and the static bare susceptibility in the constant matrix approximation for the $H1$ structure in the $1 \times 1 \times 1$ unit cell of (a)-(b) SnSe_2 and (c)-(d) SnS_2 as a function of pressure along a high-symmetry \mathbf{q} -path. The dashed and dotted lines for SnSe_2 indicate pressures at which the material is in the metallic phase⁷⁷. The $\chi_{\mathbf{q}}^{0,\text{CMA}}$ values in (b) and (d) should be multiplied by a factor of 10^4 and 10^3 , respectively.

($\Pi_{\mathbf{q}\nu}^A$) for the lowest-energy phonon mode and the static bare susceptibility in the constant matrix approximation ($\chi_{\mathbf{q}}^{0,\text{CMA}}$) using the following equations^{43,74,75}

$$\Pi_{\mathbf{q}\nu}^A = 2 \sum_{mn} \int \frac{d\mathbf{k}}{\Omega_{\text{BZ}}} \left[\frac{f_{n\mathbf{k}} - f_{m\mathbf{k}+\mathbf{q}}}{\varepsilon_{m\mathbf{k}+\mathbf{q}} - \varepsilon_{n\mathbf{k}}} \right] \times g_{mn,\nu}^b(\mathbf{k}, \mathbf{q}) \times g_{mn,\nu}^*(\mathbf{k}, \mathbf{q}) \quad (1)$$

$$\chi_{\mathbf{q}}^{0,\text{CMA}} = 2 \sum_{mn} \int \frac{d\mathbf{k}}{\Omega_{\text{BZ}}} \left[\frac{f_{n\mathbf{k}} - f_{m\mathbf{k}+\mathbf{q}}}{\varepsilon_{m\mathbf{k}+\mathbf{q}} - \varepsilon_{n\mathbf{k}}} \right] \quad (2)$$

Here, 2 is the spin degeneracy factor, $\varepsilon_{n\mathbf{k}}$ and $f_{n\mathbf{k}}$ represent single-particle energies and Fermi-Dirac occupation factors, respectively, and Ω_{BZ} is the BZ volume. The screened e-ph matrix elements $g_{mn,\nu}(\mathbf{k}, \mathbf{q})$ were obtained as $g_{mn,\nu}(\mathbf{k}, \mathbf{q}) = \langle \psi_{m\mathbf{k}+\mathbf{q}} | \partial_{\mathbf{q}\nu} V | \psi_{n\mathbf{k}} \rangle / \sqrt{\hbar/2\omega_{\mathbf{q}\nu}}$, where $\psi_{n\mathbf{k}}$ represents the Kohn-Sham single-particle eigenstates, $\partial_{\mathbf{q}\nu} V$ is the derivative of the self-consistent potential, and $\omega_{\mathbf{q}\nu}$ is the phonon frequency associated with phonon branch ν and wave vector \mathbf{q} . The bare matrix element $g_{mn,\nu}^b(\mathbf{k}, \mathbf{q})$ is calculated by multiplying the screened e-ph matrix elements $g_{mn,\nu}(\mathbf{k}, \mathbf{q})$ with the electronic dielectric function at $\omega=0$ [$\varepsilon(\mathbf{q}, \omega=0)$]. Thus, the matrix elements $g_{mn,\nu}^b(\mathbf{k}, \mathbf{q}) \times g_{mn,\nu}^*(\mathbf{k}, \mathbf{q})$ in Eqn. (1) can be replaced by $|g_{mn,\nu}(\mathbf{k}, \mathbf{q})|^2 \times \varepsilon(\mathbf{q}, \omega=0)$ ⁷⁸.

Both $\chi_{\mathbf{q}}^{0,\text{CMA}}$ and $\Pi_{\mathbf{q}\nu}^A$ are properties of the FS bands and those electronic states close to them, yet $\chi_{\mathbf{q}}^{0,\text{CMA}}$ is purely electronic, while $\Pi_{\mathbf{q}\nu}^A$ includes the fully anisotropic e-ph interaction. As can be appreciated in Fig. 7, we observe an increasing response of $\Pi_{\mathbf{q}\nu}^A$ and $\chi_{\mathbf{q}}^{0,\text{CMA}}$ at the K point in both systems with increasing pressure, meaning that both FS nesting as well as the e-ph coupling strength

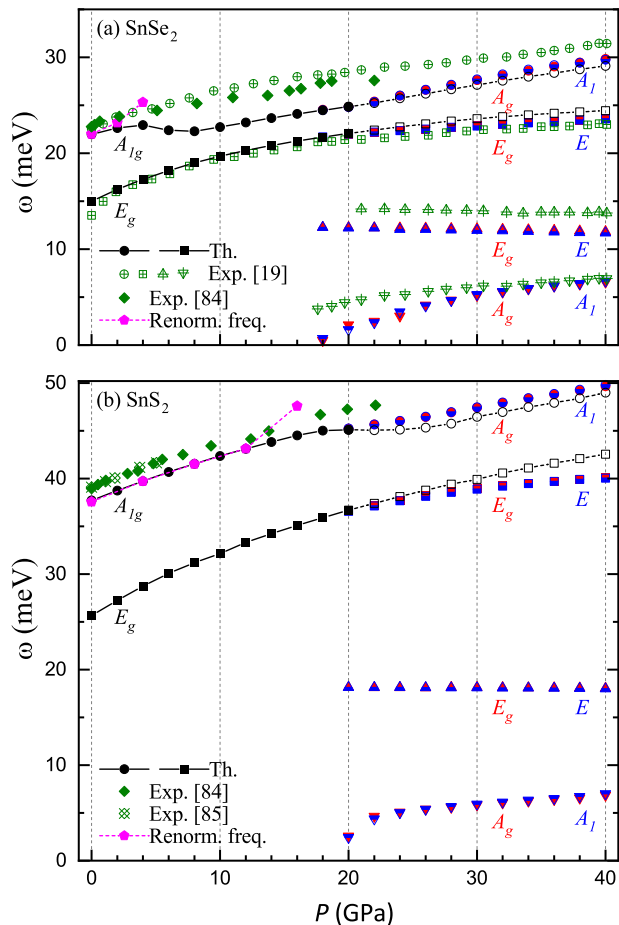


FIG. 8: Calculated frequency dependence of the Raman-active modes at Γ as a function of pressure for (a) SnSe₂ and (b) SnS₂. The theoretical results are shown as black symbols (*H1*), red symbols (*H2-1*), and blue symbols (*H2-2*) while the experimental results^{19,84,85} are shown as olive symbols. For *H1*, the data before and after the phase transition are shown as filled and open symbols. The nonadiabatically corrected frequency points are shown as filled magenta pentagons.

increase at the BZ regions close to *K* as the critical pressure for the phase transition is approached. This leads us to the conclusion that both FS nesting and strong e-ph interactions are providing important contributions in creating the PLD instability in SnS₂, in close analogy to SnSe₂^{19,76,77}.

Having identified the PLD instability in SnS₂ to be of the same origins as in SnSe₂, we carry on to compare the materials' Raman-active modes' frequencies as a function of pressure, as shown in Fig. 8. The high energy E_g mode increases monotonically as a function of pressure in both SnSe₂ and SnS₂. The high energy A_{1g} mode, on the other hand, shows a noticeable change of slope at approximately 6 and 20 GPa in the case of SnSe₂ and SnS₂, respectively. This can be related to the semiconductor-to-metal transition in both systems as also supported by Supplemental Fig. S12⁵¹. After the phase transition, due

to the in-plane tripling of the unit cell, two additional Raman-active modes appear at 17 GPa for SnSe₂ and at 20 GPa for SnS₂, in good agreement with available experimental data¹⁹.

The pressure dependence of the high-energy E_g mode for SnSe₂ is in very good agreement with the experimental results, however, the high-energy A_{1g} mode, while reproducing nicely the qualitative trend, underestimates the phonon energies by ~ 0.5 meV at 0 GPa and ~ 3 meV at 6 GPa (the metallization pressure) compared to experiments¹⁹. Recent studies on other insulators and semiconductors show that the underestimation of phonon energies with respect to experiments can be due to the neglect of nonadiabatic effects in the theoretical approach⁷⁹⁻⁸³. In order to assess the effect of nonadiabatic corrections on the phonon dispersions in our systems, we employed a field-theoretic framework⁷⁴, where the phonon self-energy $\Pi_{\mathbf{q}\nu}$ can be partitioned into adiabatic and nonadiabatic contributions, i.e., $\Pi(\omega) = \Pi^A + \Pi^{\text{NA}}(\omega)$. Thus, the nonadiabatic corrections to the self-energy as a function of the phonon mode ν and wave vector \mathbf{q} are given by:

$$\hbar\Pi_{\mathbf{q}\nu}^{\text{NA}}(\omega) = 2 \sum_{mn} \int \frac{d\mathbf{k}}{\Omega_{\text{BZ}}} \times g_{mn,\nu}^b(\mathbf{k}, \mathbf{q}) \times g_{mn,\nu}^*(\mathbf{k}, \mathbf{q}) \times \left[\frac{f_{m\mathbf{k}+\mathbf{q}} - f_{n\mathbf{k}}}{\varepsilon_{m\mathbf{k}+\mathbf{q}} - \varepsilon_{n\mathbf{k}} - \hbar(\omega + i\eta)} - \frac{f_{m\mathbf{k}+\mathbf{q}} - f_{n\mathbf{k}}}{\varepsilon_{m\mathbf{k}+\mathbf{q}} - \varepsilon_{n\mathbf{k}}} \right] \quad (3)$$

with η being a positive infinitesimal number. The nonadiabatic phonon spectral function^{86,87} can then be calculated using

$$A_{\mathbf{q}\nu}^{\text{NA}}(\omega) = \frac{1}{\pi} \text{Im} \left[\frac{2\hbar\omega_{\mathbf{q}\nu}}{(\hbar\omega)^2 - (\hbar\omega_{\mathbf{q}\nu})^2 - 2\hbar\omega_{\mathbf{q}\nu}\Pi_{\mathbf{q}\nu}^{\text{NA}}(\omega)} \right] \quad (4)$$

Equation (4) reveals that a strong response of the system is expected at the nonadiabatic phonon frequency, $\Omega_{\mathbf{q}\nu}$, when the denominator is very small or vanishes. The renormalized nonadiabatic phonon energy, that is, the phonon energy modified by the phonon self-energy of Eqn. (3) is thus given by

$$\Omega_{\mathbf{q}\nu}^2 \simeq \omega_{\mathbf{q}\nu}^2 + 2\omega_{\mathbf{q}\nu} \text{Re}\Pi_{\mathbf{q}\nu}^{\text{NA}}(\Omega_{\mathbf{q}\nu}) \quad (5)$$

The nonadiabatic spectral functions and the nonadiabatic phonon dispersions obtained via Eqns. (4) and (5) at various pressures along the $\Gamma - M - K - \Gamma$ direction for SnSe₂ and SnS₂ are reported in Fig. 9. As can be appreciated from Fig. 9, the nonadiabatic effects are very small in both systems at ambient pressure. As the pressure increases (and the band gap decreases), the renormalization of the A_{1g} mode energy becomes significant around 4 GPa in SnSe₂ and around 16 GPa in SnS₂. In particular, the A_{1g} mode in SnSe₂ hardens by ~ 2 meV at 4 GPa

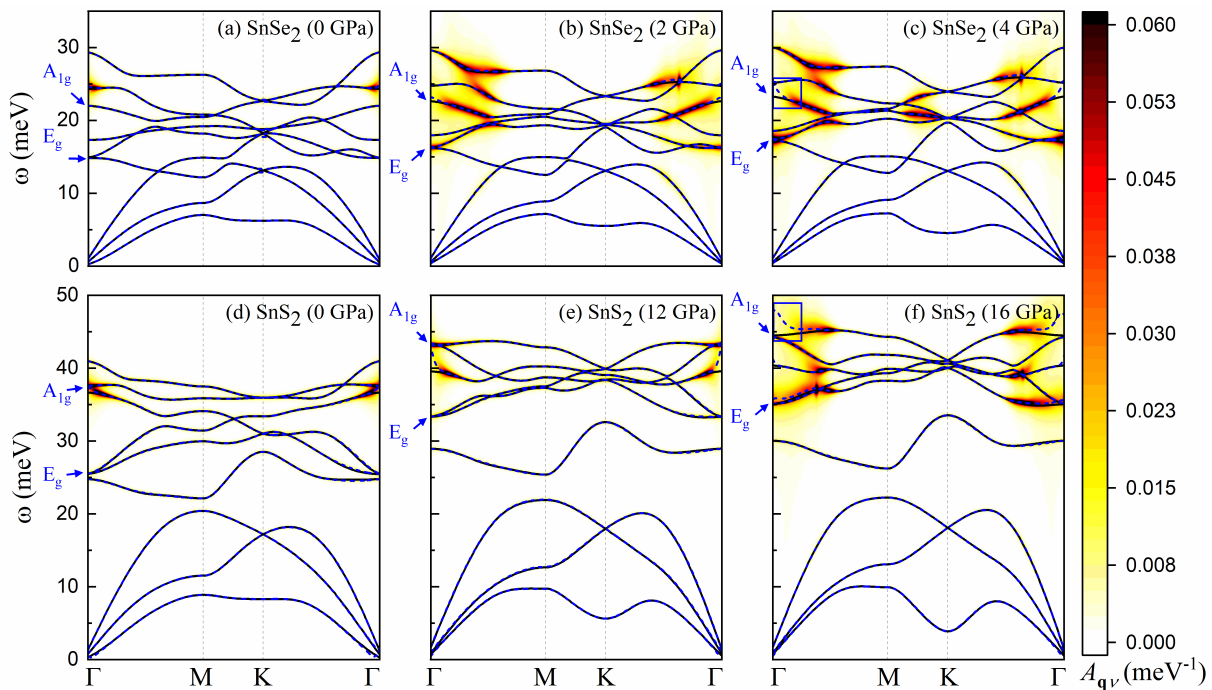


FIG. 9: Calculated nonadiabatic phonon spectral function and nonadiabatic renormalized phonon for the $H1$ structure in the $1 \times 1 \times 1$ unit cell of (a)-(c) SnSe_2 and (d)-(f) SnS_2 at various pressures. The solid black and dashed blue lines represent the DFPT phonon and renormalized phonon dispersions, respectively. The color map corresponds to the nonadiabatic phonon spectral function.

[Fig. 9(c)], improving the quantitative agreement of our calculations with the experiments¹⁹ [see also Fig. 8]. Similarly, the A_{1g} mode in SnS_2 hardens by ~ 3 meV at 16 GPa as shown in Fig. 9(f). For the E_g mode, where the agreement between experiments and theory has already been very good, the nonadiabatic corrections are found to be very small.

As SnSe_2 and SnS_2 are polar semiconductors at ambient and low pressures, we also want to address the topic of LO-TO splitting. At ambient pressure, we observe a LO-TO splitting of 7 meV for SnSe_2 and 11.8 meV for SnS_2 [see Supplemental Fig. S13⁵¹]. With increasing pressure, the band gap decreases and the value for the dielectric function increases. In turn, the magnitude of the LO-TO splitting decreases, in accordance with experimental measurements in other polar semiconductors^{88,89}. Interestingly, however, at the critical pressures above which our compounds become metallic, our calculations still yield finite values for the splitting (around 6.4 meV for SnSe_2 and 10 meV for SnS_2). A possible explanation for the residual LO-TO splitting is that in the pressure regions, where the materials pass through the semiconductor-metal phase transition, the charge carrier concentration is so low that the long-range Coulomb interactions are not fully screened, thus allowing for finite LO-TO splitting. In the fully metallic state at higher pressures, the long-range Coulomb interactions are screened completely leading to the degeneracy of LO and TO modes. Although highly interesting, resolving the intermediate bad

metal phase would go beyond the scope of this work and is therefore the focus of future investigations.

D. Superconducting properties

Experimental evidence of pressure-induced superconductivity in SnSe_2 has been recently provided based on electrical transport and synchrotron XRD measurements²⁸. The superconducting state is observed to emerge at 18.6 GPa and to reach a maximum T_c of about 6.1 K, which remains nearly constant in a large pressure range between 30.1 and 50.3 GPa. Earlier studies have demonstrated superconductivity in bulk and thin films SnSe_2 through intercalation and gating^{13,90–92} as well as interface superconductivity in SnSe_2 /ion-liquid and SnSe_2 /graphene^{93,94}.

In this section we investigate the origin of the observed superconducting transition in SnSe_2 using the Migdal-Eliashberg (ME) formalism implemented in the EPW code^{43,95}. To facilitate the comparison with the experimental results of Zhou *et al.*²⁸, the superconducting properties are calculated at the experimental unit cell parameters for nonhydrostatic pressure points at 23 and 30 GPa while allowing the atomic positions to relax. The resulting electronic structure and phonon dispersion are shown in Supplemental Figs. S14-S16⁵¹. A comparison with the plots under hydrostatic conditions at 20 and 30 GPa [Figs. 5, 6, and S3] demonstrate that the elec-

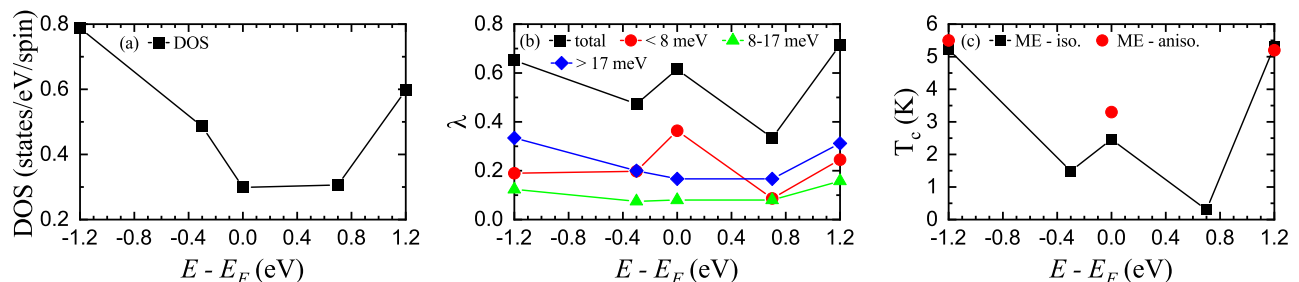


FIG. 10: Variations in (a) DOS at E_F , (b) λ , and (c) T_c as a function of a rigid shift of the Fermi level for the $H1$ structure in the $1 \times 1 \times 1$ unit cell of SnSe_2 at the experimental unit cell parameters at 23 GPa. In (b), squares represent the total λ , while circles, triangles, and rhombuses represent the contribution of the low-, medium- and high-energy modes. In (c), circles and squares represent the T_c obtained from the numerical solutions of the anisotropic and isotropic ME equations.

tronic structure is highly insensitive to the crystal structure parameters while the phonon frequencies are slightly affected. For instance, according to our phonon calculations within the harmonic approximation a lattice instability starts developing at 20 and 30 GPa under hydrostatic and nonhydrostatic conditions, respectively. Since the pressure-dependence of the lowest acoustic mode at the K point is responsible for the dynamical instability in this compound, the reduced in-plane compressibility rate in the latter case leads to a decrease in the phonon softening rate and consequently an increase in the stability region up to 30 GPa. While this trend is in the right direction, the transition pressure is still underestimated compared to the nonhydrostatic experiments in Ref. [28] that showed no structural phase transition or decomposition up to 46 GPa. The situation is reminiscent of the one encountered in NbSe_2 and NbS_2 , where the instability found at the harmonic level has been shown to be weakened or even removed when quantum anharmonic effects are taken into account, and therefore suppress the formation of the CDW phase^{16,30}. A similar scenario occurring in SnSe_2 would extend the stabilization region to higher pressures as found in experiment. To check this point, we re-evaluated the phonons at the K point with a larger smearing value of 0.03 Ry and indeed found that the imaginary phonon mode is removed, thus preserving the dynamic stability [see dash line in Supplemental Fig. S16(a)⁵¹].

In order to understand the origin of the superconducting state, we evaluate the Eliashberg spectral function $\alpha^2 F(\omega)$ and the corresponding e-ph coupling strength λ . A comparative analysis of the $\alpha^2 F(\omega)$ and the atomically resolved phonon DOS (PHDOS) at the experimental lattice cell parameters at 23 GPa [Supplemental Fig. S15⁵¹] reveals that the low-frequency phonons below 8 meV associated with both Sn and Se vibrations contribute 60% of the total $\lambda = 0.62$, while the phonons in the high-frequency region between 17 and 32 meV dominated by Se atoms vibrations give approximately 30% of λ [Fig. 10(b)]. Using a typical value of $\mu^* = 0.1$, we predict a T_c of 2.5 and 3.3 K from the numerical solutions of the isotropic and anisotropic ME gap equations^{43,95},

slightly below the 4.0 K onset temperature (T_c^{onset}) of electrical resistance drop at 22 GPa reported in Ref. [28]. The results are almost unchanged when the calculations are performed at the experimental lattice cell parameters at 30 GPa [Supplemental Fig. S16⁵¹]. For the K point phonons computed at the larger smearing value of 0.03 Ry, we get $\lambda = 0.59$ and an isotropic $T_c = 2.3$ K with $\mu^* = 0.1$.

Considering that superconductivity in SnSe_2 has been achieved experimentally either in Se-deficient²⁸ or intercalated^{13,90-92} samples, we further investigate the impact of doping on the predicted T_c via a rigid shift of E_F , chosen to match particular features either in the valence or in the conduction band, for the structure at the experimental lattice cell parameters at 23 GPa. The results summarized in Fig. 10 can be rationalized in terms of the changes taking place at the FS upon raising or lowering the Fermi level. In the undoped systems, the momentum-resolved e-ph coupling strength $\lambda_{\mathbf{k}}$ on the FS displays a highly anisotropic distribution (between 0.3 and 1.1) where the lower and upper regions of the spectra can be associated with the Γ and K -centered pockets, respectively [Fig. 11(a),(c)]. A continuous distribution with a sizable anisotropy is also found for the superconducting gap on the FS as shown in Fig. 11(b),(d). When E_F is moved up by 0.7 eV, the spread in $\lambda_{\mathbf{k}}$ is reduced to a much narrower range of 0.3-0.5 since the Γ -centered hole-like FS sheet vanishes. However, the spread goes back to the wider range once the system is doped until the Fermi level matches the first peak in the conduction band DOS as two additional FS sheets are introduced, thus opening extra scattering channels. This leads to an enhancement in both $\lambda = 0.72$ and $T_c \approx 5.2$ K, the latter in good agreement with the maximum T_c value found experimentally. Similar trends are also observed when the Fermi level is shifted down. It is also worth noting that the non-linear dependence of the total λ with doping correlates closely with that of the low-energy phonons [Fig. 10], indicating that these modes play a decisive role in raising the e-ph coupling strength and T_c in this system.

For completeness, we also analyze the superconducting properties of SnS_2 . Assuming that the dynamical

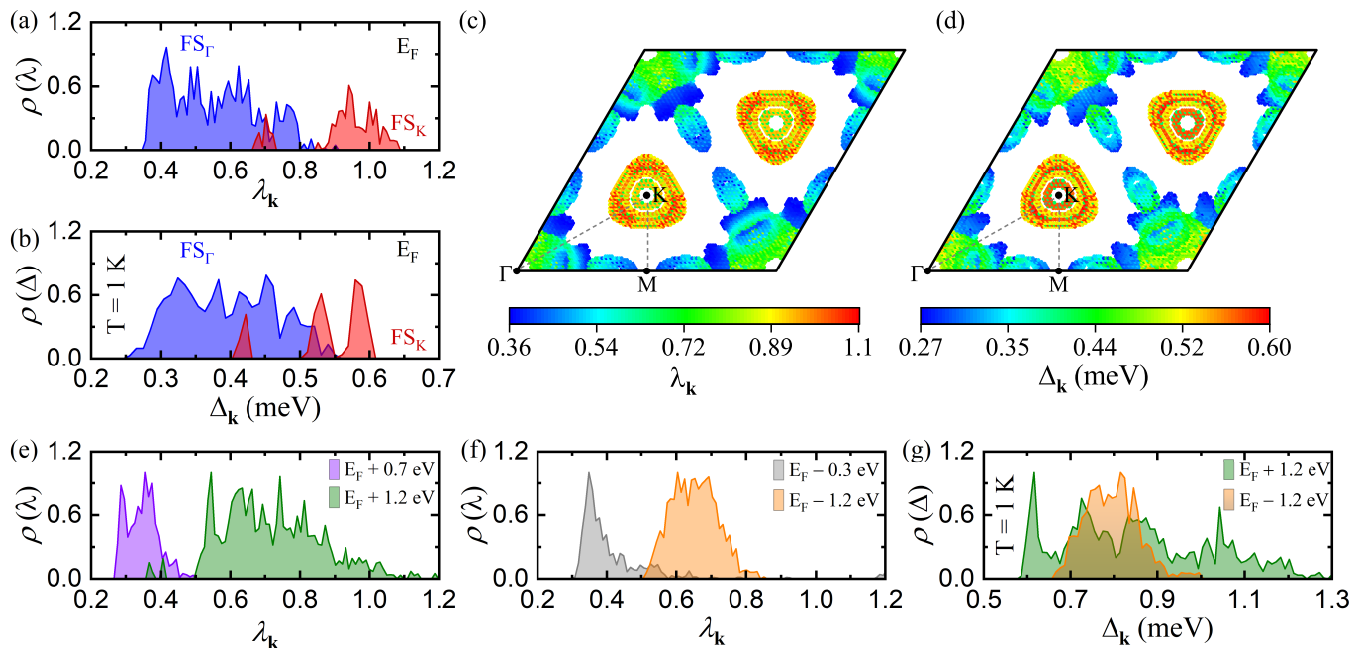


FIG. 11: Calculated superconducting properties for the $H1$ structure in the $1 \times 1 \times 1$ unit cell of SnSe_2 at the experimental unit cell parameters at 23 GPa. Energy distribution of the (a) e-ph coupling strength $\lambda_{\mathbf{k}}$ and (b) superconducting gap $\Delta_{\mathbf{k}}$; color coded by FS sheets: Γ -centered holelike pocket FS_{Γ} (blue), and K -centered electronlike pocket FS_K (red). Momentum-resolved (c) e-ph coupling strength $\lambda_{\mathbf{k}}$ and (d) superconducting gap $\Delta_{\mathbf{k}}$ on the FS (top-view). Energy distribution of the (e) e-ph coupling strength $\lambda_{\mathbf{k}}$, and (f), (g) superconducting gap $\Delta_{\mathbf{k}}$ at $T = 1$ K at various rigid shifts of the Fermi level with respect to the original data as shown in Supplemental Fig. S14⁵¹.

stability of SnS_2 can be extended to higher pressures under nonhydrostatic compression as for SnSe_2 , we perform superconductivity calculations at 30 GPa and used a smearing value of 0.04 Ry for the phonons at the K point in order to remove the imaginary frequency. The calculated PHDOS and Eliashberg spectral function comprise of two well defined regions separated by a gap between the acoustic and optical branches [Supplemental Fig. S18⁵¹]. Integrating $\alpha^2 F(\omega)$, the strength of the e-ph coupling λ is estimated to be 1.08. From the solutions of the isotropic and anisotropic ME gap equations with $\mu^* = 0.1$, we obtain a T_c of 4.6 and 5.9 K, respectively [Supplemental Figs. S19-S20⁵¹]. The values of λ and T_c are twice larger than those in SnSe_2 due to the enhanced coupling of the acoustic phonons dominated by Sn vibrations with the electronic state present at the Fermi level. Similar to SnSe_2 , the strongest coupling takes place on the K -centered FS, but both $\lambda_{\mathbf{k}}$ and $\Delta_{\mathbf{k}}$ exhibit a much broader distribution profile. We also find that λ is strongly affected by changes in the FS topology when E_F is shifted up or down. Namely, the e-ph coupling drops significantly as the contribution of the low-energy acoustic modes is drastically reduced and large doping is required to raise back the T_c .

Finally, we investigate SnSe_2 and SnS_2 compounds in the $H2-1$ structure as potential superconductors. The results are presented in Supplemental Figs. S21-S23⁵¹. Despite the close resemblance between the DOS and PH-

DOS of the parent and superlattice structures, the T_c in $H2-1$ phase is found to be an order of magnitude lower than in the $H1$ phase. This can be linked to a decrease in the e-ph coupling over the full phonon range due to the reorganization that takes place at the FS. Looking at the electronic band structure in the $\sqrt{3} \times \sqrt{3} \times 1$ supercell [region enclosed by the green box in Fig. 6], it can be seen that the Γ -centered FS sheet disappears as a gap opens in the electronic band dominated by Se p_z orbitals. An increase in the DOS at E_F is expected to produce a marked enhancement in T_c , particularly under hole doping as multiple bands will cross the Fermi level. In SnSe_2 a 0.3 eV down shift in E_F results in an isotropic $T_c = 3.7$ K, while in SnS_2 a 0.5 eV down shift leads to $T_c = 3.5$ K.

IV. CONCLUSIONS

In this work, we have performed a comparative study of SnSe_2 and SnS_2 at ambient conditions and pressures up to 40 GPa. We show that the apparent contradictions among high-pressure results on SnSe_2 can be attributed to differences in experimental conditions and that inclusion of nonadiabatic effects improves the quantitative agreement with the measured Raman-active phonon frequencies. We further demonstrate that a periodic lattice transition, of a similar origin to the one observed

in SnSe₂, also occurs in SnS₂ above 20 GPa. In addition, we examine the nature of the superconducting state recently observed in SnSe₂ under nonhydrostatic pressure, and provide evidence that the superconducting transition can be explained within a standard phonon-mediated mechanism. The emergence of superconductivity with a comparable critical temperature in SnS₂ under similar experimental conditions is also predicted. Finally, we show that in the high pressure PLD *H2-1* phase the T_c is reduced by an order of magnitude compared to the high-symmetry *H1* phase in both systems, a fact that we attribute to a restructuring and suppression of large parts of the Fermi surface.

Conflicts of interest

There are no conflicts to declare.

Acknowledgments

The authors thank J. Ying, V. V. Struzhkin, and F. Caruso for useful discussions. C. H. acknowledges support by the Austrian Science Fund (FWF) Project No. P32144-N36 and the VSC-3 of the Vienna University of Technology. G. P. K., H. P., and E. R. M. acknowledge support from the National Science Foundation (Award No. OAC-1740263). This work used Spiedie cluster at Binghamton University and Comet cluster at the San Diego Supercomputer Center through allocation TG-DMR180071. Comet is a dedicated XSEDE cluster⁹⁶, which is supported by National Science Foundation Grant No. ACI-1548562.

-
- * Electronic address: rmargine@binghamton.edu
- ¹ F. Ke, J. Yang, C. Liu, Q. Wang, Y. Li, J. Zhang, L. Wu, X. Zhang, Y. Han, B. Wu, Y. Ma, and C. Gao, “High-pressure electrical-transport properties of SnS: experimental and theoretical approaches”, *J. Phys. Chem. C* **117**, 6033 (2013).
 - ² J. Vidal, S. Lany, M. d’Avezac, A. Zunger, A. Zakutayev, J. Francis, and J. Tate, “Band-structure, optical properties, and defect physics of the photovoltaic semiconductor SnS”, *Appl. Phys. Lett.* **100**, 032104 (2012).
 - ³ P. Sinsersuksakul, L. Sun, S. W. Lee, H. H. Park, S. B. Kim, C. Yang, and R. G. Gordon, “Overcoming efficiency limitations of SnS-based solar cells”, *Adv. Energy Mater.* **4**, 1400496 (2014).
 - ⁴ L.-D. Zhao, S.-H. Lo, Y. Zhang, H. Sun, G. Tan, C. Uher, C. Wolverton, V. P. Dravid, and M. G. Kanatzidis, “Ultra-low thermal conductivity and high thermoelectric figure of merit in SnSe crystals”, *Nature* **508**, 373 (2014).
 - ⁵ G. Ding, G. Gao, and K. Yao, “High-efficient thermoelectric materials: The case of orthorhombic IV-VI compounds”, *Sci. Rep.* **5**, 9567 (2015).
 - ⁶ H. Yu, S. Dai, and Y. Chen, “Enhanced power factor via the control of structural phase transition in SnSe”, *Sci. Rep.* **6**, 26193 (2016).
 - ⁷ L. D. Zhao, G. Tan, S. Hao, J. He, Y. Pei, H. Chi, H. Wang, S. Gong, H. Xu, V. P. Dravid, C. Uher, “Ultra-high power factor and thermoelectric performance in hole-doped single-crystal SnSe”, *Science* **351**, 141 (2016).
 - ⁸ A. Dewandre, O. Hellman, S. Bhattacharya, A. H. Romero, G. K. H. Madsen, and M. J. Verstraete, “Two-step phase transition in SnSe and the origins of its high power factor from first principles”, *Phys. Rev. B* **117**, 276601 (2016).
 - ⁹ X. Chen, P. Lu, X. Wang, Y. Zhou, C. An, Y. Zhou, C. Xian, H. Gao, Z. Guo, C. Park, B. Hou, K. Peng, X. Zhou, J. Sun, Y. Xiong, Z. Yang, D. Xing, and Y. Zhang, “Topological Dirac line nodes and superconductivity coexist in SnSe at high pressure”, *Phys. Rev. B* **96**, 165123 (2017).
 - ¹⁰ H. Yu, W. Lao, L. Wang, K. Li, and Y. Chen, “Pressure-stabilized tin selenide phase with an unexpected stoichiometry and a predicted superconducting state at low temperatures”, *Phys. Rev. Lett.* **118**, 137002 (2017).
 - ¹¹ G. Marini, P. Barone, A. Sanna, C. Tresca, L. Benfatto, and G. Profeta, “Superconductivity in tin selenide under pressure”, *Phys. Rev. Mater.* **3**, 114803 (2019).
 - ¹² J. Zhou, S. Zhang, and J. Li, “Normal-to-topological insulator martensitic phase transition in group-IV monochalcogenides driven by light”, *NPG Asia Mater.* **12**, 1 (2020).
 - ¹³ H. Wu, S. Li, M. Susner, S. Kwon, M. Kim, T. Haugan, B. Lv, “Spacing dependent and cation doping independent superconductivity in intercalated 1T two dimensional SnSe₂”, *2D Mater.* **6**, 045048. (2019).
 - ¹⁴ Y. Qi, P. G. Naumov, M. N. Ali, C. R. Rajamathi, W. Schnelle, O. Barkalov, M. Hanfland, S.-C. Wu, C. Shekhar, Y. Sun, V. Süß, M. Schmidt, U. Schwarz, E. Pippel, P. Werner, R. Hillebrand, T. Förster, E. Kampert, S. Parkin, R. J. Cava, C. Felser, B. Yan, and S. A. Medvedev, “Superconductivity in Weyl semimetal candidate MoTe₂”, *Nat. Commun.* **7**, 11038 (2016).
 - ¹⁵ X. C. Pan, X. Chen, H. Liu, Y. Feng, Z. Wei, Y. Zhou, Z. Chi, L. Pi, F. Yen, F. Song, X. Wan, Z. Yang, B. Wang, G. Wang, and Y. Zhang, “Pressure-driven dome-shaped superconductivity and electronic structural evolution in tungsten ditelluride”, *Nat. Commun.* **6**, 7805 (2015).
 - ¹⁶ M. Leroux, I. Errea, M. L. Tacon, S.-M. Souliou, G. Garbarino, L. Cario, A. Bosak, F. Mauri, M. Calandra, and P. Rodiere, “Strong anharmonicity induces quantum melting of charge density wave in 2H-NbSe₂ under pressure”, *Phys. Rev. B* **92**, 140303 (2015).
 - ¹⁷ B. Sipoš, A. F. Kusmartseva, A. Akrap, H. Berger, L. Forró, and E. Tutiš, “From Mott state to superconductivity in 1T-TaS₂”, *Nat. Mater.* **7**, 960 (2008).
 - ¹⁸ H. Paudyal, S. Poncé, F. Giustino, and E. R. Margine, “Superconducting properties of MoTe₂ from *ab initio* anisotropic Migdal-Eliashberg theory”, *Phys. Rev. B* **101**, 214515 (2020).
 - ¹⁹ J. Ying, H. Paudyal, C. Heil, X. J. Chen, V. V. Struzhkin, and E. R. Margine, “Unusual pressure-induced periodic lattice distortion in SnSe₂”, *Phys. Rev. Lett.* **121**, 027003

- (2018).
- 20 M. Calandra and F. Mauri, “Charge-density wave and superconducting dome in TiSe_2 from electron-phonon interaction”, *Phys. Rev. Lett.* **106**, 196406 (2011).
 - 21 M. N. Ali, J. Xiong, S. Flynn, J. Tao, Q. D. Gibson, L. M. Schoop, T. Liang, N. Haldolaarachchige, M. Hirschberger, N. P. Ong, and R. J. Cava, “Large, non-saturating magnetoresistance in WTe_2 ”, *Nature* **514**, 205 (2014).
 - 22 K. Nguyen-Cong, J. M. Gonzalez, B. A. Steele, I. I. Oleynik, “Tin-Selenium compounds at ambient and high pressures”, *J. Phys. Chem.* **122**, 18274 (2018).
 - 23 J. M. Gonzalez, K. Nguyen-Cong, B. A. Steele, and I. I. Oleynik, “Novel phases and superconductivity of tin sulfide compounds”, *J. Chem. Phys.* **148**, 194701 (2018).
 - 24 Y. A. Timofeev, B. V. Vinogradov, and V. B. Begoulev, “Superconductivity of tin selenide at pressures up to 70 GPa”, *Phys. Solid State* **39**, 207 (1997).
 - 25 A. H. C. Neto, “Charge density wave, superconductivity, and anomalous metallic behavior in 2D transition metal dichalcogenides”, *Phys. Rev. Lett.* **86**, 4382 (2001).
 - 26 D. Kang, Y. Zhou, W. Yi, C. Yang, J. Guo, Y. Shi, S. Zhang, Z. Wang, C. Zhang, S. Jiang, A. Li, K. Yang, Q. Wu, G. Zhang, L. Sun, and Z. Zhao, “Superconductivity emerging from a suppressed large magnetoresistant state in tungsten ditelluride”, *Nat. Commun.* **6**, 7804 (2015).
 - 27 T. Valla, A. V. Fedorov, P. D. Johnson, P.-A. Glans, C. McGuinness, K. E. Smith, E. Y. Andrei, and H. Berger, “Quasiparticle spectra, charge-density waves, superconductivity, and electron-phonon coupling in 2H-NbSe_2 ”, *Phys. Rev. Lett.* **92**, 086401 (2004).
 - 28 Y. Zhou, B. Zhang, X. Chen, C. Gu, C. An, Y. Zhou, K. Cai, Y. Yuan, C. Chen, H. Wu, R. Zhang, C. Park, Y. Xiong, X. Zhang, K. Wang, and Z. Yang, “Pressure-induced metallization and robust superconductivity in pristine 1T-SnSe_2 ”, *Adv. Electron. Mater.* **4**, 1800155 (2018).
 - 29 W. Albers and K. Schol, “The P-T-X phase diagram of the system Sn-S”, *Philips Res. Repts.* **16**, 329 (1961).
 - 30 C. Heil, S. Ponc e, H. Lambert, M. Schlipf, E. R. Margine, and F. Giustino, “Origin of superconductivity and latent charge density wave in NbS_2 ”, *Phys. Rev. Lett.* **119**, 087003 (2017).
 - 31 M. Calandra, I. Mazin, and F. Mauri, “Effect of dimensionality on the charge-density wave in few-layer 2H-NbSe_2 ”, *Phys. Rev. B* **80**, 241108 (2009).
 - 32 M. D. Johannes and I. I. Mazin, “Fermi surface nesting and the origin of charge density waves in metals”, *Phys. Rev. B* **77**, 165135 (2008).
 - 33 F. Weber, S. Rosenkranz, J.-P. Castellan, R. Osborn, R. Hott, R. Heid, K.-P. Bohnen, T. Egami, A. H. Said, and D. Reznik, “Extended phonon collapse and the origin of the charge-density wave in 2H-NbSe_2 ”, *Phys. Rev. Lett.* **107**, 107403 (2011).
 - 34 P. Giannozzi, O. Andreussi, T. Brumme, O. Bunau, M. B. Nardelli, M. Calandra, R. Car, C. Cavazzoni, D. Ceresoli, M. Cococcioni *et al.*, “Advanced capabilities for materials modelling with Quantum ESPRESSO”, *J. Phys.: Condens. Matter* **29**, 465901 (2017).
 - 35 D. R. Hamann, “Optimized norm-conserving Vanderbilt pseudopotentials”, *Phys. Rev. B* **88**, 085117 (2013).
 - 36 J. P. Perdew, K. Burke, and M. Ernzerhof, “Generalized gradient approximation made simple”, *Phys. Rev. Lett.* **77**, 3865 (1996).
 - 37 J. Klimeš, D. R. Bowler, and A. Michaelides, “Van der Waals density functionals applied to solids”, *Phys. Rev. B* **83**, 195131 (2011).
 - 38 J. Klimeš, D. R. Bowler, and A. Michaelides, “Chemical accuracy for the van der Waals density functional”, *J. Phys.: Condens. Matter* **22**, 022201 (2010).
 - 39 N. Marzari, D. Vanderbilt, A. De Vita, and M. Payne, “Thermal contraction and disordering of the Al (110) surface”, *Phys. Rev. Lett.* **82**, 3296 (1999).
 - 40 H. J. Monkhorst and J. D. Pack, “Special points for Brillouin-zone integrations”, *Phys. Rev. B* **13**, 5188 (1976).
 - 41 S. Baroni, S. de Gironcoli, A. D. Corso, and P. Giannozzi, “Phonons and related crystal properties from density-functional perturbation theory”, *Rev. Mod. Phys.* **73**, 515 (2001).
 - 42 F. Giustino, M. L. Cohen, and S. G. Louie, “Electron-phonon interaction using Wannier functions”, *Phys. Rev. B* **76**, 165108 (2007).
 - 43 S. Ponc e, E. R. Margine, C. Verdi, and F. Giustino, “EPW: Electron-phonon coupling, transport and superconducting properties using maximally localized Wannier functions”, *Comput. Phys. Commun.* **209**, 116 (2016).
 - 44 N. Marzari, A. A. Mostofi, J. R. Yates, I. Souza, and D. Vanderbilt, “Maximally localized Wannier functions: Theory and applications”, *Rev. Mod. Phys.* **84**, 1419 (2012).
 - 45 G. Pizzi, V. Vitale, R. Arita, S. Bluegel, F. Freimuth, G. G eranton, M. Gibertini, D. Gresch, C. Johnson, T. Koretune *et al.*, “Wannier90 as a community code: new features and applications”, *J. Phys.: Condens. Matter* (2019).
 - 46 Y. Huang, E. Sutter, J. T. Sadowski, M. Cotlet, O. L. Monti, D. A. Rucke, M. R. Neupane, D. Wickramaratne, R. K. Lake, B. A. Parkinson, and P. Sutter, “Tin disulfide—an emerging layered metal dichalcogenide semiconductor: materials properties and device characteristics”, *ACS Nano* **8**, 10743 (2014).
 - 47 Z. V. Borges, C. M. Poffo, J. C. de Lima, S. M. Souza, D. M. Trich s, and R. S. de Biasi, “High-pressure angle-dispersive X-ray diffraction study of mechanically alloyed SnSe_2 ”, *J. Appl. Phys.* **124**, 215901 (2018).
 - 48 K. Knorr, L. Ehm, M. Hytha, B. Winkler, and W. Depmeier, “The High pressure behaviour of SnS_2 : X-Ray powder diffraction and quantum mechanical calculations up to 10 GPa”, *Phys. Stat. Sol.* **223**, 435 (2001).
 - 49 R. M. Hazen, L. W. Finger, “The crystal structures and compressibilities of layer minerals at high pressure. I. SnS_2 , berndtite”, *American Mineralogist* **63**, 289 (1978).
 - 50 M.  . Fils , E. Eikeland, J. Zhang, S. R. Madsen and B. B. Iversen, “Atomic and electronic structure transformations in SnS_2 at high pressures: a joint single crystal X-ray diffraction and DFT study”, *Dalton Trans.* **45**, 3798 (2016).
 - 51 See Supplemental Material at [url] for Figs. S1-S23 and Table S1.
 - 52 L. Yang, L. Dai, H. Li, H. Hu, K. Liu, C. Pu, M. Hong, and P. Liu, “Pressure-induced metallization in MoSe_2 under different pressure conditions”, *RSC Adv.* **9**, 5794 (2019).
 - 53 S. Duwal and C.-S. Yoo, “Shear-induced isostructural phase transition and metallization of layered tungsten disulfide under nonhydrostatic compression”, *J. Phys. Chem. C* **120**, 5101 (2016).
 - 54 M. Fujimoto, “The Physics of Structural Phase Transitions”, Springer-Verlag New York, second edition, (2005).
 - 55 A. N. Kolmogorov, S. Shah, E. R. Margine, A. K. Kleppe,

- and A. P. Jephcoat, “Pressure-driven evolution of the covalent network in CaB_6 ”, *Phys. Rev. Lett.* **109**, 075501 (2012).
- ⁵⁶ S. Hajinazar, A. Thorn, E. D. Sandoval, S. Kharabade, and A. N. Kolmogorova, “MAISE: Construction of neural network interatomic models and evolutionary structure optimization”, arXiv:2005.12131v2.
- ⁵⁷ S. Shah and A. N. Kolmogorov, “Stability and superconductivity of Ca-B phases at ambient and high pressure”, *Phys. Rev. B* **88**, 014107 (2013).
- ⁵⁸ J. Gusakova, X. Wang, L. L. Shiau, A. Krivosheeva, V. Shaposhnikov, V. Borisenko, V. Gusakov, and B. K. Tay, “Electronic properties of bulk and monolayer TMDs: theoretical study within DFT framework (GVJ-2e method)”, *Phys. Status Solidi A* **214**, 1700218 (2017).
- ⁵⁹ A. Zunger and A. J. Freeman, “Band structure and lattice mobility of TiSe_2 ”, *Phys. Rev. B* **17**, 1839 (1978).
- ⁶⁰ F. J. Di Salvo, D. E. Moncton, and J. V. Waszczak, “Electronic properties and superlattice formation in the semimetal TiSe_2 ”, *Phys. Rev. B* **14**, 4321 (1976).
- ⁶¹ A. H. Reshak and S. Auluck, “Electronic and optical properties of the 1T phases of TiS_2 , TiSe_2 , and TiTe_2 ”, *Phys. Rev. B* **68**, 245113 (2003).
- ⁶² G. Domingo, R. S. Itoga, and C. R. Kannewurf, “Fundamental optical absorption in SnS_2 , and SnSe_2 ”, *Phys. Rev.* **143**, 536 (1966).
- ⁶³ L. A. Burton, T. J. Whittles, D. Hesp, W. M. Linhart, J. M. Skelton, B. Hou, R. F. Webster, G. O’Dowd, C. Reece, D. Cherns, D. J. Fermin, T. D. Veal, V. R. Dhanak, and A. Walsh, “Electronic and optical properties of single crystal SnS_2 : an earth-abundant disulfide photocatalyst”, *J. Mater. Chem. A* **4**, 1312 (2016).
- ⁶⁴ P. Manou, J.A. Kalomiro, A.N. Anagnostopoulos, and K. Kambas, “Optical properties of SnSe_2 single crystals”, *Phys. Rev.* **143**, 536 (1966).
- ⁶⁵ Y. Kumagai, L. A. Burton, A. Walsh, and F. Oba, “Electronic Structure and Defect Physics of Tin Sulfides: SnS , Sn_2S_3 , and SnS_2 ”, *Phys. Rev. Appl.* **6**, 014009 (2016).
- ⁶⁶ Z. R. Kudrynskiy, X. Wang, J. Sutcliffe, M. A. Bhuiyan, Y. Fu, Z. Yang, O. Makarovskiy, L. Eaves, A. Solomon, V. T. Maslyuk, Z. D. Kovalyuk, L. Zhang, and A. Patané, “Van der Waals $\text{SnSe}_{2(1-x)}\text{S}_{2x}$ alloys: composition-dependent bowing coefficient and electron-phonon interaction”, *Adv. Funct. Mater.* **30**, 1908092 (2020).
- ⁶⁷ J. M. Gonzalez and I. I. Oleynik, “Layer-dependent properties of SnS_2 and SnSe_2 two-dimensional materials”, *Phys. Rev. B* **94**, 125443 (2016).
- ⁶⁸ H. Guo, T. Yang, P. Tao, Y. Wang, and Z. Zhang, “High pressure effect on structure, electronic structure, and thermoelectric properties of MoS_2 ”, *J. Appl. Phys.* **113**, 013709 (2013).
- ⁶⁹ V. Rajaji, U. Dutta, P. C. Sreeparvathy, S. Ch. Sarma, Y. A. Sorb, B. Joseph, S. Sahoo, S. C. Peter, V. Kanchana, and C. Narayana, “Structural, vibrational, and electrical properties of 1T- TiTe_2 under hydrostatic pressure: experiments and theory”, *Phys. Rev. B* **97**, 085107 (2018).
- ⁷⁰ A. P. Nayak, S. Bhattacharyya, J. Zhu, J. Liu, X. Wu, T. Pandey, C. Jin, A. K. Singh, D. Akinwande, and J.-F. Lin, “Pressure-induced semiconducting to metallic transition in multilayered molybdenum disulphide”, *Nat. Commun.* **5**, 1 (2014).
- ⁷¹ L. Zhang, Y. Xie, T. Cui, Y. Li, Z. He, Y. Ma, and G. Zou, “Pressure-induced enhancement of electron-phonon coupling in superconducting CaC_6 from first principles”, *Phys. Rev. B* **74**, 184519 (2006).
- ⁷² J. S. Kim, L. Boeri, and R. K. Kremer, and F. S. Razavi, “Effect of pressure on superconducting Ca-intercalated graphite CaC_6 ”, *Phys. Rev. B* **74**, 214513 (2006).
- ⁷³ M. Calandra, A. N. Kolmogorov, and S. Curtarolo, “Search for high T_c in layered structures: The case of LiB”, *Phys. Rev. B* **75**, 144506 (2007).
- ⁷⁴ F. Giustino, “Electron-phonon interactions from first principles”, *Rev. Mod. Phys.* **89**, 015003 (2017).
- ⁷⁵ P. Zhang, S. G. Louie, and M. L. Cohen, “Nonlocal Screening, Electron-Phonon Coupling, and Phonon Renormalization in Metals”, *Phys. Rev. Lett.* **94**, 225502 (2005).
- ⁷⁶ We want to note at this point that there has been a mistake in the calculation of $\Pi_{\mathbf{q}\nu}^A$ and $\chi_{\mathbf{q}}^{0,\text{CMA}}$ in Ref. 19, related to the wannierization of the Fermi surface bands. We have repeated all calculations and found that while the corrected results differ quantitatively, the qualitative characteristics and the conclusions drawn remain valid.
- ⁷⁷ In the case of those pressures, where SnSe_2 is in the metallic phase, $g_{mn,\nu}^b(\mathbf{k}, \mathbf{q}) \times g_{mn,\nu}^*(\mathbf{k}, \mathbf{q})$ has been approximated using the standard expression $|g_{mn,\nu}(\mathbf{k}, \mathbf{q})|^2$ due to the fact that $\varepsilon(\mathbf{q}, \omega = 0)$ diverges for metals.
- ⁷⁸ Due to the layered structure of the considered compounds, the dielectric function exhibits a slight anisotropy with respect to its in-plane and out-of-plane components, as shown in Supplemental Fig. S13⁵¹. The differences between calculations using the in-plane, the out-of-plane or an average of the two are negligible. For simplicity and consistency, all results presented in the paper were therefore obtained using the in-plane value of the dielectric function.
- ⁷⁹ S. Pisana, M. Lazzeri, C. Casiraghi, K. S. Novoselov, A. K. Geim, A. C. Ferrari, and F. Mauri, “Breakdown of the adiabatic Born-Oppenheimer approximation in graphene”, *Nat. Mater.* **6**, 198 (2007).
- ⁸⁰ N. Caudal, A. M. Saitta, M. Lazzeri, and F. Mauri, “Kohn anomalies and nonadiabaticity in doped carbon nanotubes”, *Phys. Rev. B* **75**, 115423 (2007).
- ⁸¹ M. Calandra, M. Lazzeri, and F. Mauri, “Anharmonic and nonadiabatic effects in MgB_2 : Implications for the isotope effect and interpretation of Raman spectra”, *Physica C* **456**, 38 (2007).
- ⁸² A. M. Saitta, M. Lazzeri, M. Calandra, and F. Mauri, “Giant Nonadiabatic Effects in Layer Metals: Raman Spectra of Intercalated Graphite Explained”, *Phys. Rev. Lett.* **100**, 226401 (2008).
- ⁸³ M. Calandra, G. Profeta, and F. Mauri, “Adiabatic and nonadiabatic phonon dispersion in a Wannier function approach”, *Phys. Rev. B* **82**, 165111 (2010).
- ⁸⁴ S. V. Bhatt, M. P. Deshpande, V. Sathe, S. H. Chaki, “Effect of pressure and temperature on Raman scattering and an anharmonicity study of tin dichalcogenide single crystals”, *Solid State Commun.* **201**, 54 (2015).
- ⁸⁵ A. N. Utyuzh, Y. A. Timofeev, and G. N. Stepanov, “Effect of pressure on raman spectra of SnS_2 single crystals”, *Phys. Solid State* **52**, 352 (2010).
- ⁸⁶ P. B. Allen, “Neutron spectroscopy of superconductors”, *Phys. Rev. B* **6**, 2577 (1972).
- ⁸⁷ F. Caruso, M. Hoesch, P. Achatz, J. Serrano, M. Krisch, E. Bustarret, and F. Giustino, “Nonadiabatic Kohn Anomaly in Heavily Boron-Doped Diamond”, *Phys. Rev. Lett.* **119**, 017001 (2017).
- ⁸⁸ J.-M. Wagner and F. Bechstedt, “Pressure dependence of the dielectric and lattice-dynamical properties of GaN and AlN”, *Phys. Rev. B* **62**, 4526 (2000).

- ⁸⁹ A. R. Goñi, H. Siegle, K. Syassen, C. Thomsen, and J.-M. Wagner, “Effect of pressure on optical phonon modes and transverse effective charges in GaN and AlN”, *Phys. Rev. B* **64**, 035205 (2001).
- ⁹⁰ D. O’Hare, H. V. Wong, S. Hazell, J. W. Hodby, “Relatively isotropic superconductivity at 8.3 K in the Lamellar organometallic intercalate $\text{SnSe}_2\{\text{Co}(\eta\text{-C}_5\text{H}_5)_2\}_{0.3}$ ”, *Adv. Mater.* **4**, 658 (1992).
- ⁹¹ Z. Li, Y. Zhao, K. Mu, H. Shan, Y. Guo, J. Wu, Y. Su, Q. Wu, Z. Sun, A. Zhao, X. Cui, C. Wu, and Y. Xie, “Molecule-confined engineering toward superconductivity and ferromagnetism in two-dimensional superlattice”, *J. Am. Chem. Soc.* **139**, 16398 (2017).
- ⁹² Y. Song, X. Liang, J. Guo, J. Deng, G. Gao, and X. Chen, “Superconductivity in Li-intercalated 1T-SnSe₂ driven by electric field gating”, *Phys. Rev. Mater.* **3**, 054804 (2019).
- ⁹³ J. Zeng, E. Liu, Y. Fu, Z. Chen, C. Pan, C. Wang, M. Wang, Y. Wang, K. Xu, S. Cai, X. Yan, Y. Wang, X. Liu, P. Wang, S. J. Liang, Y. Cui, H. Y. Hwang, H. Yuan, and F. Miao, “Gate-induced interfacial superconductivity in 1T-SnSe₂”, *Nano Lett.* **18**, 1410 (2018).
- ⁹⁴ Y. M. Zhang, J. Q. Fan, W. L. Wang, D. Zhang, L. Wang, W. Li, K. He, C. L. Song, X. C. Ma, and Q. K. Xue, “Observation of interface superconductivity in a SnSe₂/epitaxial graphene van der Waals heterostructure”, *Phys. Rev. B* **98**, 220508(R) (2018).
- ⁹⁵ E. R. Margine and F. Giustino, “Anisotropic Migdal-Eliashberg theory using Wannier functions”, *Phys. Rev. B* **87**, 024505 (2013).
- ⁹⁶ J. Towns, T. Cockerill, M. Dahan, I. Foster, K. Gaither, A. Grimshaw, V. Hazlewood, S. Lathrop, D. Lifka, G. D. Peterson, R. Roskies, J. R. Scott, and N. Wilkins-Diehr, “XSEDE: Accelerating scientific discovery”, *Comput. Sci. Eng.* **16**, 62 (2014).

Supplemental Material

Electronic, vibrational, and electron-phonon coupling properties in SnSe₂ and SnS₂ under pressure

Gyanu Prasad Kafle,¹ Christoph Heil,² Hari Paudyal,¹ and Elena R. Margine^{1,*}

¹Department of Physics, Applied Physics, and Astronomy,
Binghamton University-SUNY, Binghamton, New York 13902, USA

²Institute of Theoretical and Computational Physics,
Graz University of Technology, NAWI Graz, 8010 Graz, Austria

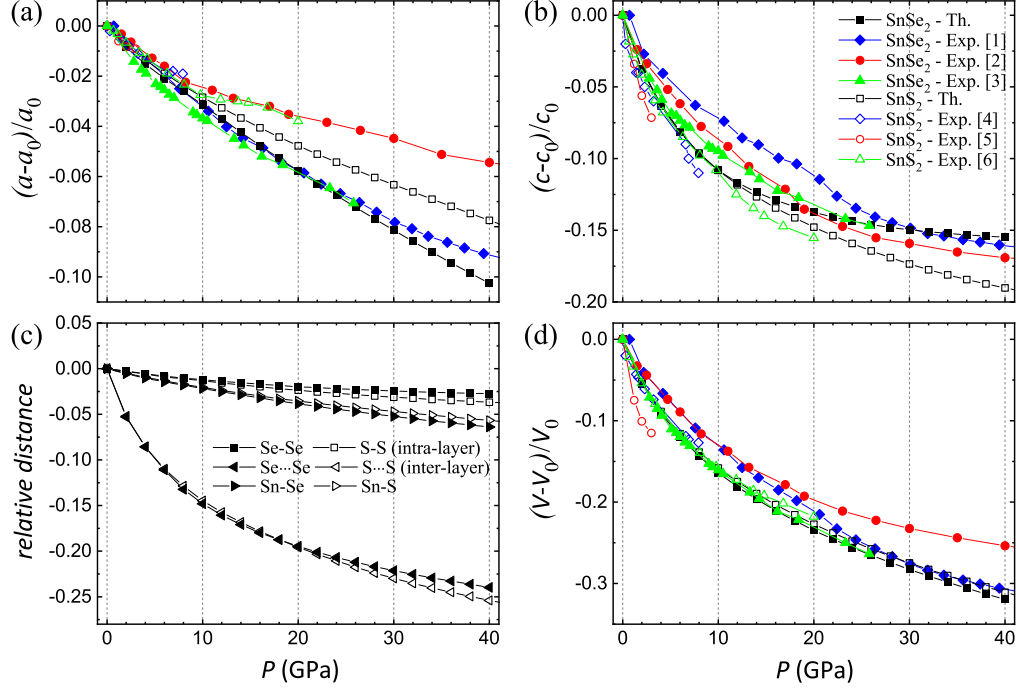


FIG. S1. Pressure dependence of the relative change of (a)-(b) lattice parameters a and c , (c) average bond lengths, and (d) volume per formula unit for SnSe₂ and SnS₂. Theoretical results are shown as black symbols and are compared with available experimental data [1–6].

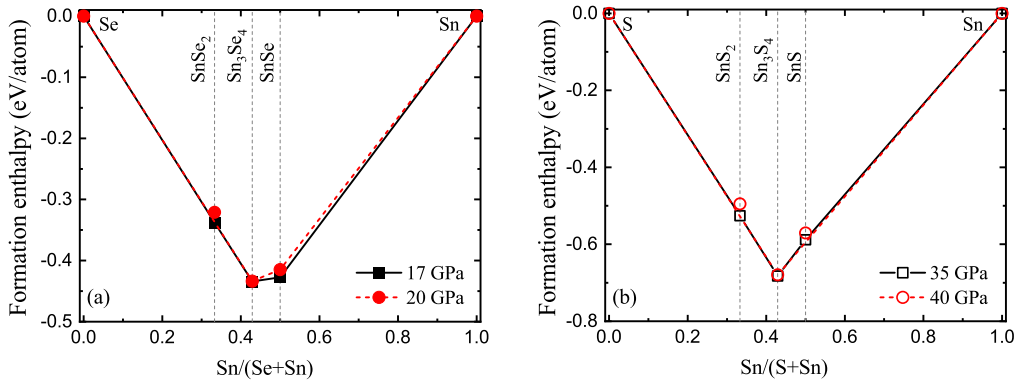


FIG. S2. Convex hulls of (a) Sn_xSe_y and (b) Sn_xS_y systems at various pressures.

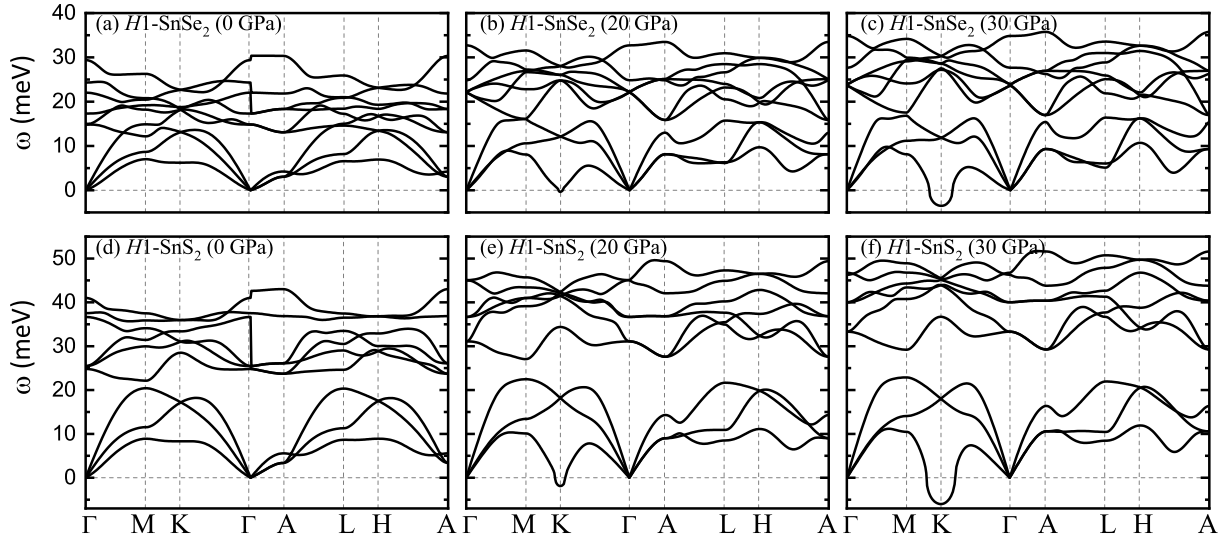


FIG. S3. Calculated phonon dispersion for the $H1$ structure in the $1 \times 1 \times 1$ unit cell of (a)-(c) SnSe_2 and (d)-(f) SnS_2 at 0, 20, and 30 GPa.

System	Phase	Space group	Eigenvector combination	ΔH (meV/atom)	Similarity factor	a (Å)	c (Å)	Wyckoff positions	
								Sn	Se/S
SnSe_2	$H1$ (0 GPa)	164 $P\bar{3}m1$				3.86169	6.10587	1a (0.00000, 0.00000, 0.00000)	2d (0.33333, 0.66667, 0.23363)
	$H1$ (30 GPa)	164 $P\bar{3}m1$				3.54726	5.19218	1a (0.00000, 0.00000, 0.00000)	2d (0.33333, 0.66667, 0.30816)
	$H2-1$ (30 GPa)	147 $P\bar{3}$	e_1	-1.86477	0.4983	6.14654	5.17350	2d (0.33333, 0.66667, 0.95799)	6g (0.02978, 0.34880, 0.30584)
	$H2-2$ (30 GPa)	157 $P31m$	e_2	-1.83621	0.2058	6.14662	5.17334	2b (0.33333, 0.66667, 0.97571)	3c (0.00000, 0.35864, 0.30583)
								1a (0.00000, 0.00000, 0.04855)	3c (0.00000, 0.69306, 0.69416)
SnS_2	$H1$ (0 GPa)	164 $P\bar{3}m1$				3.68056	5.88359	1a (0.00000, 0.00000, 0.00000)	2d (0.33333, 0.66667, 0.25197)
	$H1$ (30 GPa)	164 $P\bar{3}m1$				3.45051	4.84234	1a (0.00000, 0.00000, 0.00000)	2d (0.33333, 0.66667, 0.30146)
	$H2-1$ (30 GPa)	147 $P\bar{3}$	e_1	-1.30561	0.6158	5.96638	4.84894	2d (0.33333, 0.66667, 0.03189)	6g (0.97915, 0.32334, 0.30017)
								1a (0.00000, 0.00000, 0.00000)	
	$H2-2$ (30 GPa)	157 $P31m$	e_2	-1.31027	0.4223	5.96619	4.84884	2b (0.33333, 0.66667, 0.01870)	3c (0.00000, 0.31459, 0.30014)
							1a (0.00000, 0.00000, 0.96262)	3c (0.00000, 0.64879, 0.69986)	
$H2-3$ (30 GPa)	143 $P3$	$e_1 + e_2$	-1.32715	0.5887	5.97630	4.84268	1a (0.00000, 0.00000, 0.97419)	3d (0.99372, 0.31659, 0.30144)	
							1b (0.33333, 0.66667, 0.02175)	3d (0.00628, 0.65620, 0.69856)	
							1c (0.66667, 0.33333, 0.00407)		

TABLE S1. Space groups, lattice parameters, and Wyckoff positions of SnSe_2 and SnS_2 structures fully relaxed at the DFT level. The space groups were found with the SPGLIB tool [7] interfaced with the MAISE package [8] using a tolerance of 0.01. The lattice parameters are given for $H1$ at 0 GPa and 30 GPa, and for the $H2$ derivatives at 30 GPa. The $H2$ derivatives were constructed from the $\sqrt{3} \times \sqrt{3} \times 1$ $H1$ supercell by considering nonequivalent combinations of the e_1 and e_2 eigenvectors corresponding to the two nearly degenerate lowest-energy phonon modes A_{2g} and A_{2u} . Configuration $H2-1$ corresponds to atomic displacements along e_1 , configuration $H2-2$ corresponds to atomic displacements along e_2 , and configuration $H2-3$ corresponds to atomic displacements along a linear combination of the two eigenvectors. The similarity factor was calculated for each $H2$ derivative with respect to the undistorted $\sqrt{3} \times \sqrt{3} \times 1$ $H1$ supercell.

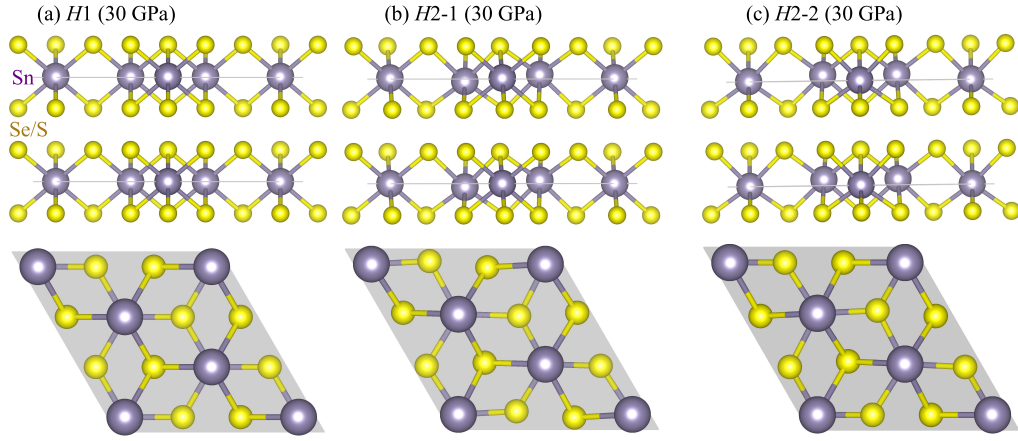


FIG. S4. Crystal structures (side and top view) for the (a) $H1$, (b) $H2-1$, and (c) $H2-2$ structures in the $\sqrt{3} \times \sqrt{3} \times 1$ supercell of SnSe_2 and SnS_2 , fully relaxed with the DFT at 30 GPa.

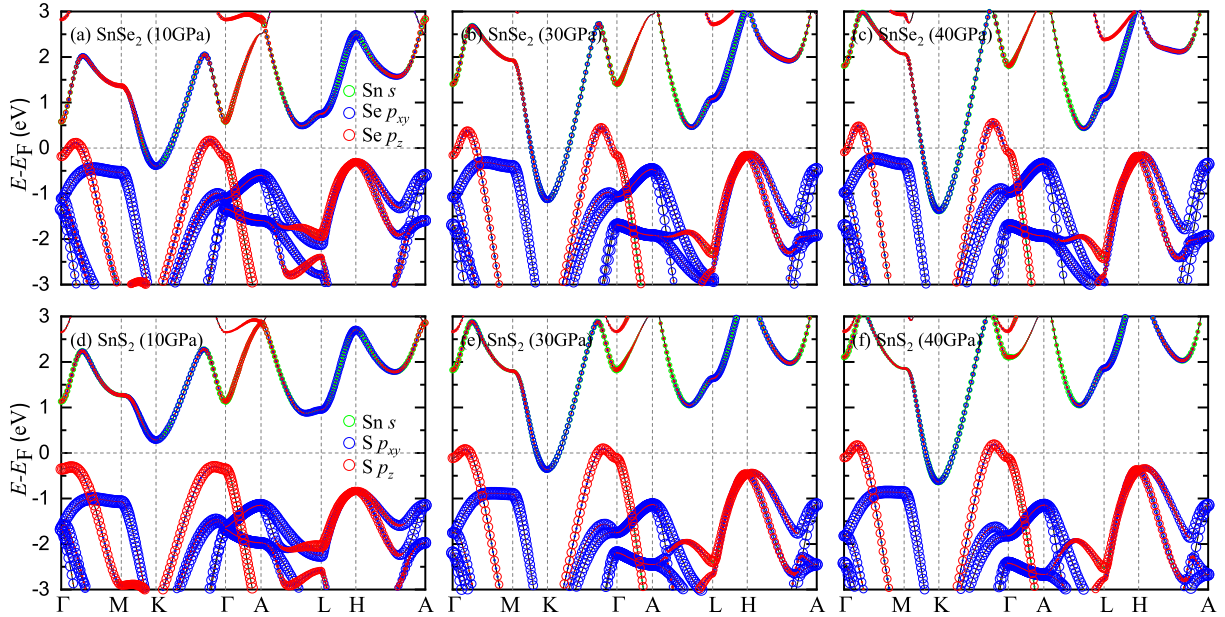


FIG. S5. Calculated band structure for the $H1$ structure in the $1 \times 1 \times 1$ unit cell of (a)-(c) SnSe_2 and (d)-(f) SnS_2 at 10, 30, and 40 GPa. The size of the symbols is proportional to the contribution of each orbital character.

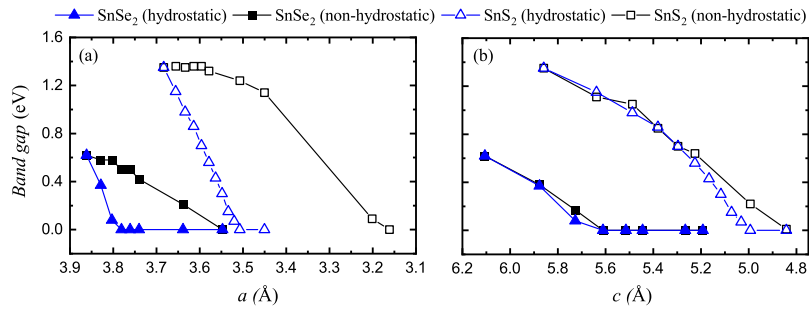


FIG. S6. Calculated band gap for the $H1$ structure in the $1 \times 1 \times 1$ unit cell of SnSe_2 and SnS_2 under hydrostatic and non-hydrostatic pressure as a function of lattice parameters (a) a and (b) c . In (a), c is kept fixed at $c = 6.10 \text{ \AA}$ for SnSe_2 and $c = 5.86 \text{ \AA}$ for SnS_2 . In (b), a is kept fixed at $a = 3.86 \text{ \AA}$ for SnSe_2 and $a = 3.68 \text{ \AA}$ for SnS_2 .

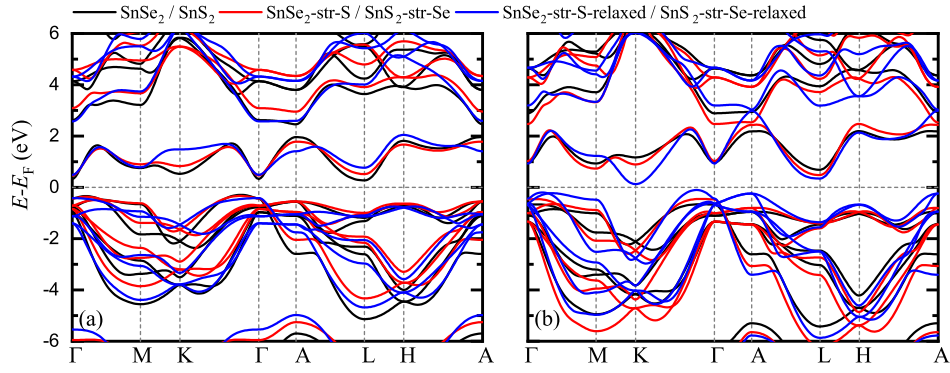


FIG. S7. Calculated band structure for the $H1$ structure in the $1 \times 1 \times 1$ unit cell of (a) SnSe_2 , $\text{SnSe}_2\text{-str-S}$, and $\text{SnSe}_2\text{-str-S-relaxed}$ and (b) SnS_2 , $\text{SnS}_2\text{-str-Se}$, and $\text{SnS}_2\text{-str-Se-relaxed}$ at 0 GPa.

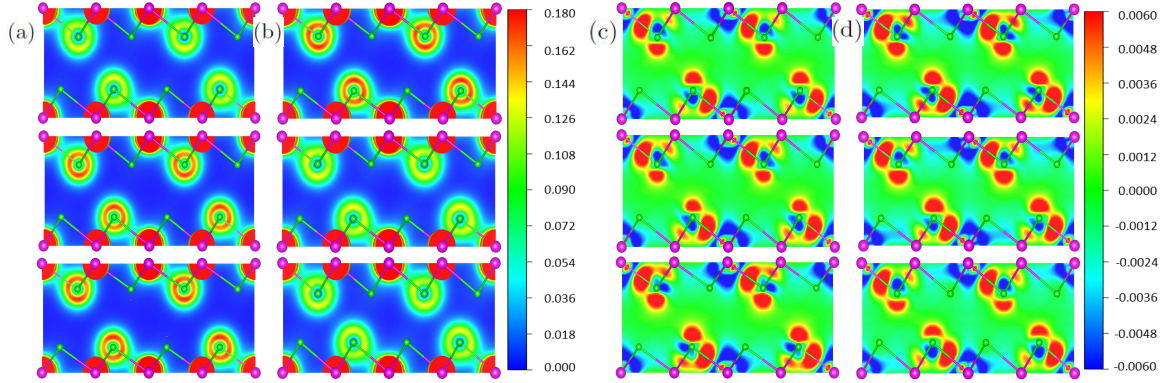


FIG. S8. Calculated (a) charge density and (c) charge density difference along the (110) plane for the $H1$ structure in the $1 \times 1 \times 1$ unit cell of SnSe_2 , $\text{SnSe}_2\text{-str-S}$, and $\text{SnSe}_2\text{-str-S-relaxed}$ (from top to bottom) at 0 GPa. Same for SnS_2 , $\text{SnS}_2\text{-str-Se}$, and $\text{SnS}_2\text{-str-Se-relaxed}$ in (b) and (d).

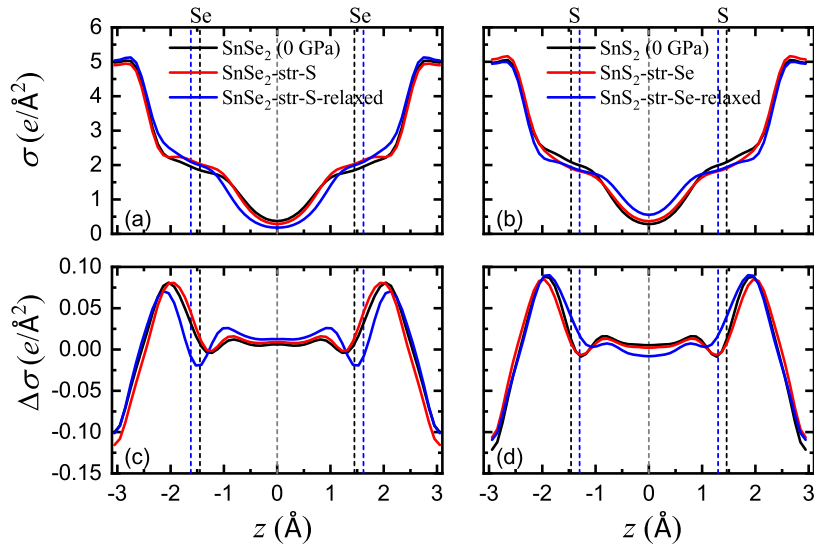


FIG. S9. Calculated (a) charge density and (c) charge density difference (in the $x-y$ plane) as a function of the perpendicular direction z for the $H1$ structure in the $1 \times 1 \times 1$ unit cell of SnSe_2 , $\text{SnSe}_2\text{-str-S}$, and $\text{SnSe}_2\text{-str-S-relaxed}$ at 0 GPa. Same for SnS_2 , $\text{SnS}_2\text{-str-Se}$, and $\text{SnS}_2\text{-str-Se-relaxed}$ in (b) and (d). The vertical black and blue dashed lines represent the position of the Se/S atoms for $\text{SnSe}_2/\text{SnS}_2$ and $\text{SnSe}_2\text{-str-S-relaxed}/\text{SnS}_2\text{-str-Se-relaxed}$ structures along c -axis, and the vertical gray dashed line represents the middle of van der Waals gap.

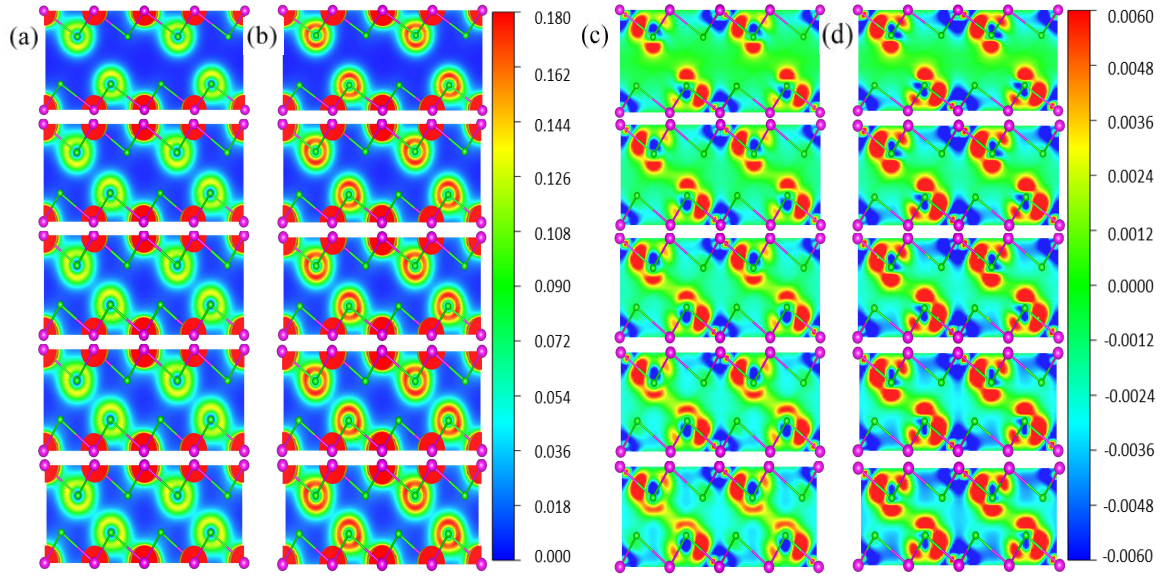


FIG. S10. Calculated (a) charge density and (c) charge density difference along the (110) plane for the *H1* structure in the $1 \times 1 \times 1$ unit cell of SnSe₂ at various pressures. Same for SnS₂ in (b) and (d). The pressure order is 0, 10, 20, 30, and 40 GPa from top to bottom.

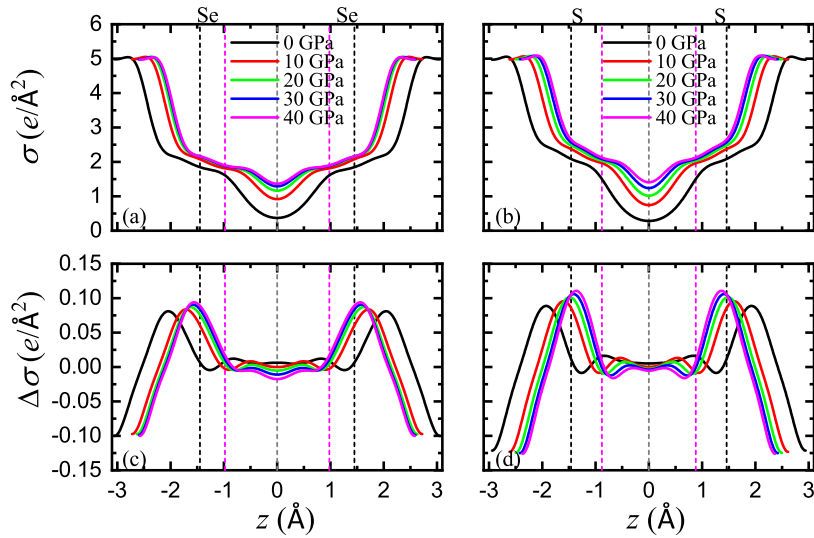


FIG. S11. Calculated (a) charge density and (c) charge density difference (in the x - y plane) as a function of the perpendicular direction z for the *H1* structure in the $1 \times 1 \times 1$ unit cell of SnSe₂ at various pressures. Same for SnS₂ in (b) and (d). The vertical black and magenta dashed lines represent the position of the Se/S atoms for SnSe₂/SnS₂ structures along c -axis at 0 and 40 GPa, respectively, and the vertical gray dashed line represents the middle of van der Waals gap.

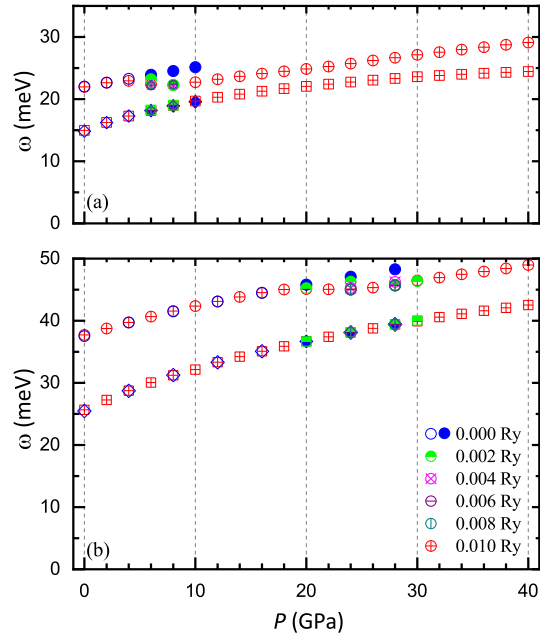


FIG. S12. Calculated frequency dependence of the Raman-active modes, A_{1g} and E_g , for the $H1$ structure in the $1 \times 1 \times 1$ unit cell of (a) SnSe₂ and (b) SnS₂ as a function of pressure using various smearing values. The data before and after the metalization (6 GPa in SnSe₂ and 20 GPa in SnS₂) using no smearing are shown as open and filled blue circles, respectively.

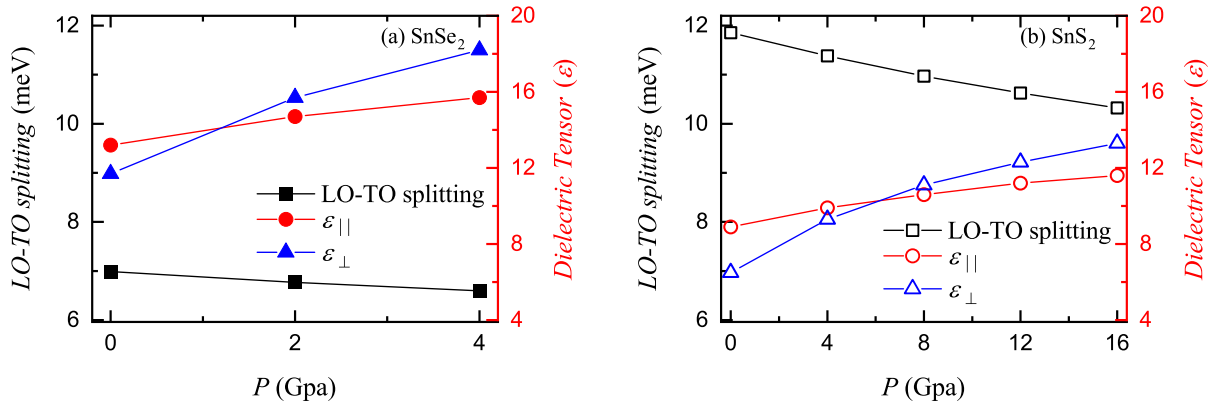


FIG. S13. Calculated LO-TO splitting, and in-plane ($\epsilon_{||}$) and out-of-plane (ϵ_{\perp}) dielectric tensors for the $H1$ structure in the $1 \times 1 \times 1$ unit cell of (a) SnSe₂ and (b) SnS₂ as a function of pressure.

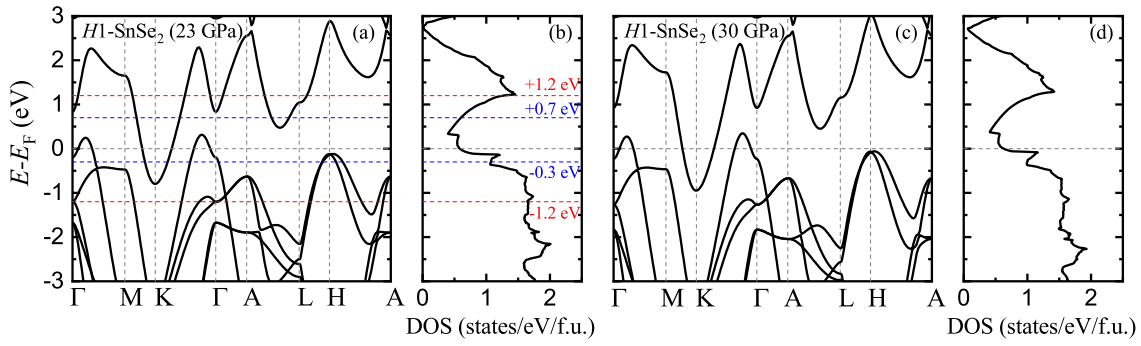


FIG. S14. Calculated band structure and DOS for the *H1* structure in the $1 \times 1 \times 1$ unit cell of SnSe₂ at the experimental unit cell parameters at (a)-(b) 23 and (c)-(d) 30 GPa. The red and blue dashed lines represent rigid shifts of the Fermi level with respect to the original data.

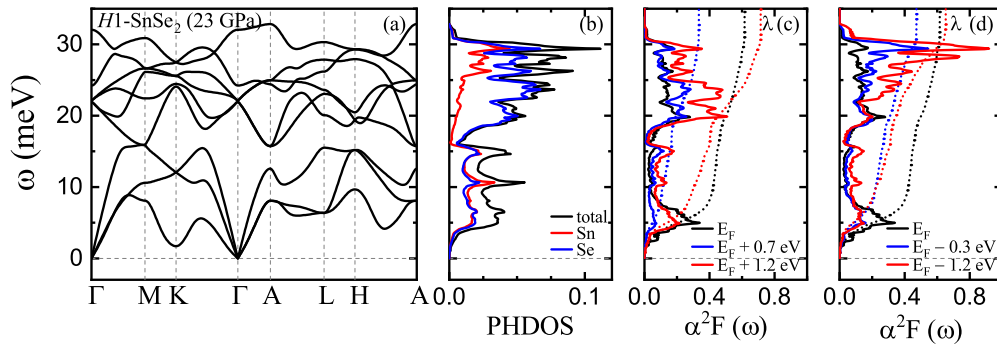


FIG. S15. Calculated (a) phonon dispersion, (b) PHDOS, and (c)-(d) Eliashberg spectral function $\alpha^2F(\omega)$ and e-ph coupling strength $\lambda(\omega)$ for the *H1* structure in the $1 \times 1 \times 1$ unit cell of SnSe₂ at the experimental lattice parameters at 23 GPa. In (c) and (d), black lines show $\alpha^2F(\omega)$ and $\lambda(\omega)$ at the Fermi level, while red and blue lines show the same quantities for the rigid shifts in the Fermi level indicated in Fig. S14(a)-(b).

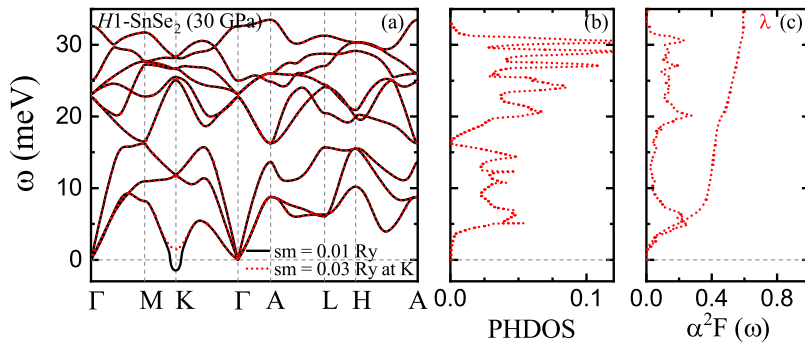


FIG. S16. Calculated (a) phonon dispersion, (b) PHDOS, and (c) Eliashberg spectral function $\alpha^2F(\omega)$, and e-ph coupling strength $\lambda(\omega)$ for the *H1* structure in the $1 \times 1 \times 1$ unit cell of SnSe₂ at the experimental lattice parameters at 30 GPa. The black lines represent the phonon calculated with a smearing value of 0.01 Ry, while red lines with a smearing value of 0.03 Ry at the *K*-point in the BZ.

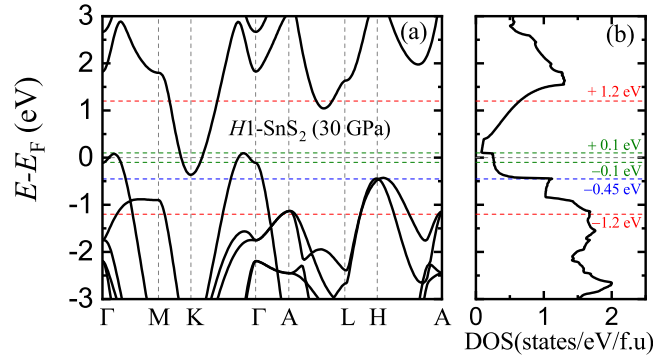


FIG. S17. Calculated (a) band structure and (b) DOS for the $H1$ structure in the $1 \times 1 \times 1$ unit cell of SnS_2 at 30 GPa. The red and blue dashed lines represent rigid shifts of the Fermi level with respect to the original data.

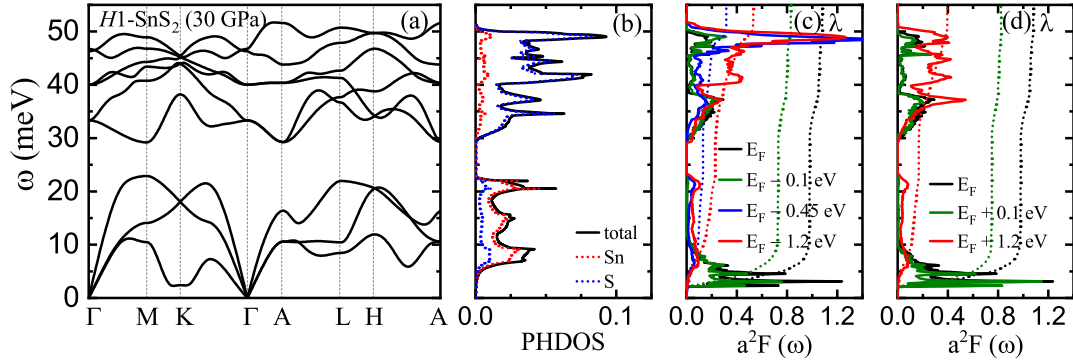


FIG. S18. Calculated (a) phonon dispersion, (b) PHDOS, and (c)-(d) Eliashberg spectral function $\alpha^2 F(\omega)$, and e-ph coupling strength $\lambda(\omega)$ for the $H1$ structure in the $1 \times 1 \times 1$ unit cell of SnS_2 at 30 GPa. In (c) and (d), black lines show $\alpha^2 F(\omega)$ and $\lambda(\omega)$ at the Fermi level, while red, blue and green lines show the same quantities for the rigid shifts in the Fermi level indicated in Fig. S17. The phonon is calculated with a smearing value of 0.04 Ry at the K -point in the BZ.

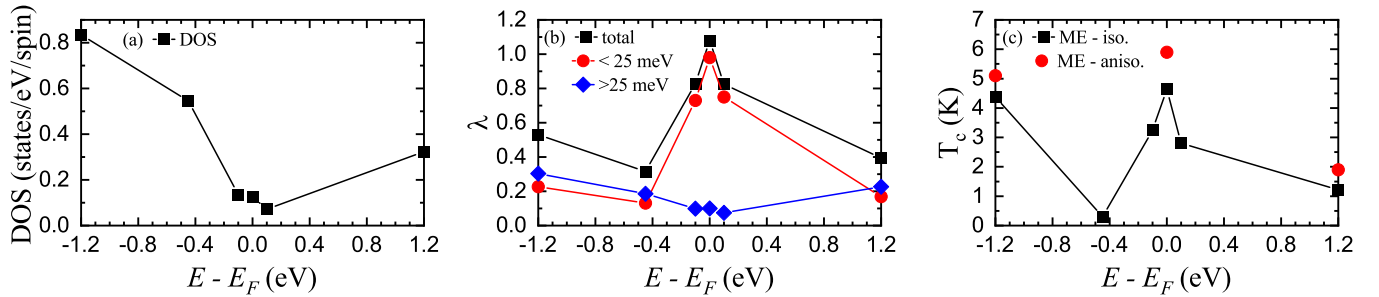


FIG. S19. Variations in (a) DOS at E_F , (b) λ , and (c) T_c as a function of a rigid shift of the Fermi level for the $H1$ structure in the $1 \times 1 \times 1$ unit cell of SnS_2 at 30 GPa. In (b), squares represent the total λ , while circles and rhombuses represent the contribution of the low- and high-energy modes. In (c), circles and squares represent the T_c obtained from the numerical solutions of the anisotropic and isotropic ME equations.

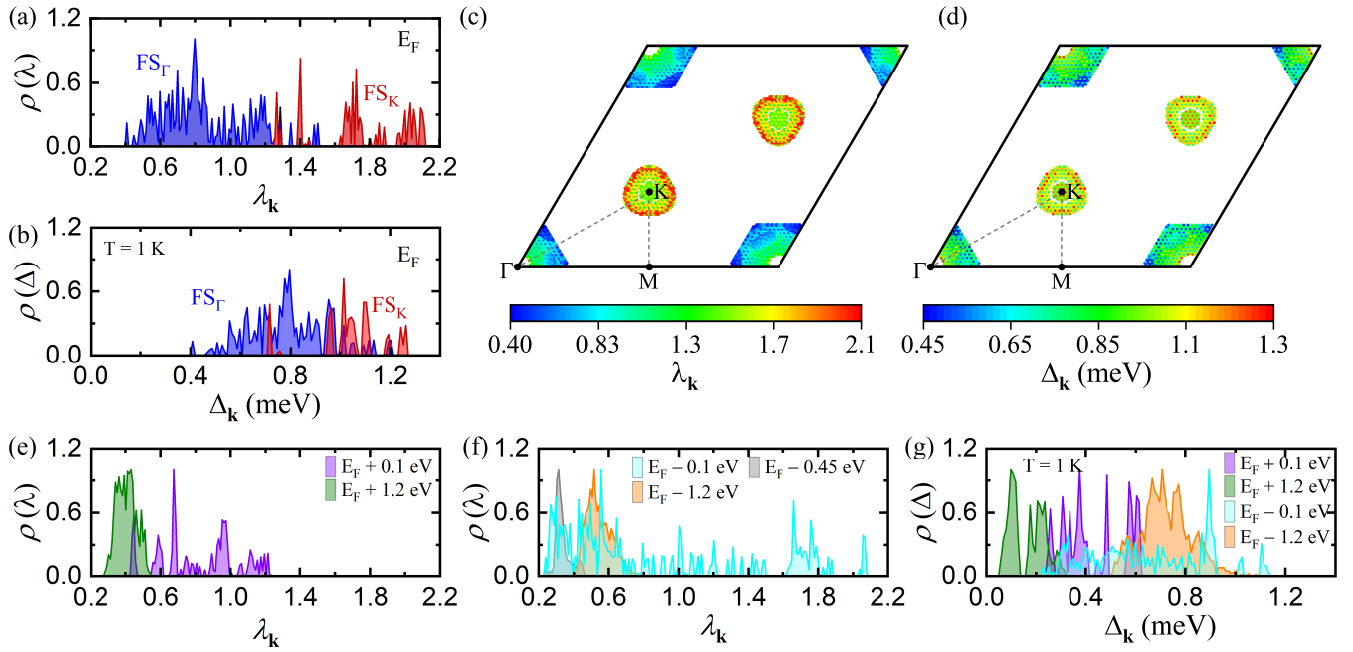


FIG. S20. Calculated superconducting properties for the $H1$ structure in the $1 \times 1 \times 1$ unit cell of SnS_2 at 30 GPa. Energy distribution of the (a) e-ph coupling strength $\lambda_{\mathbf{k}}$ and (b) superconducting gap $\Delta_{\mathbf{k}}$; color coded by FS sheets: Γ -centered holelike pocket FS_{Γ} (blue), and K -centered electronlike pocket FS_K (red). Momentum-resolved (c) e-ph coupling strength $\lambda_{\mathbf{k}}$ and (d) superconducting gap $\Delta_{\mathbf{k}}$ on the FS (top-view). Energy distribution of the (e) e-ph coupling strength $\lambda_{\mathbf{k}}$, and (f)-(g) superconducting gap $\Delta_{\mathbf{k}}$ at $T = 1$ K at various rigid shifts of the Fermi level with respect to the original data as shown in Fig. S17(a)-(b).

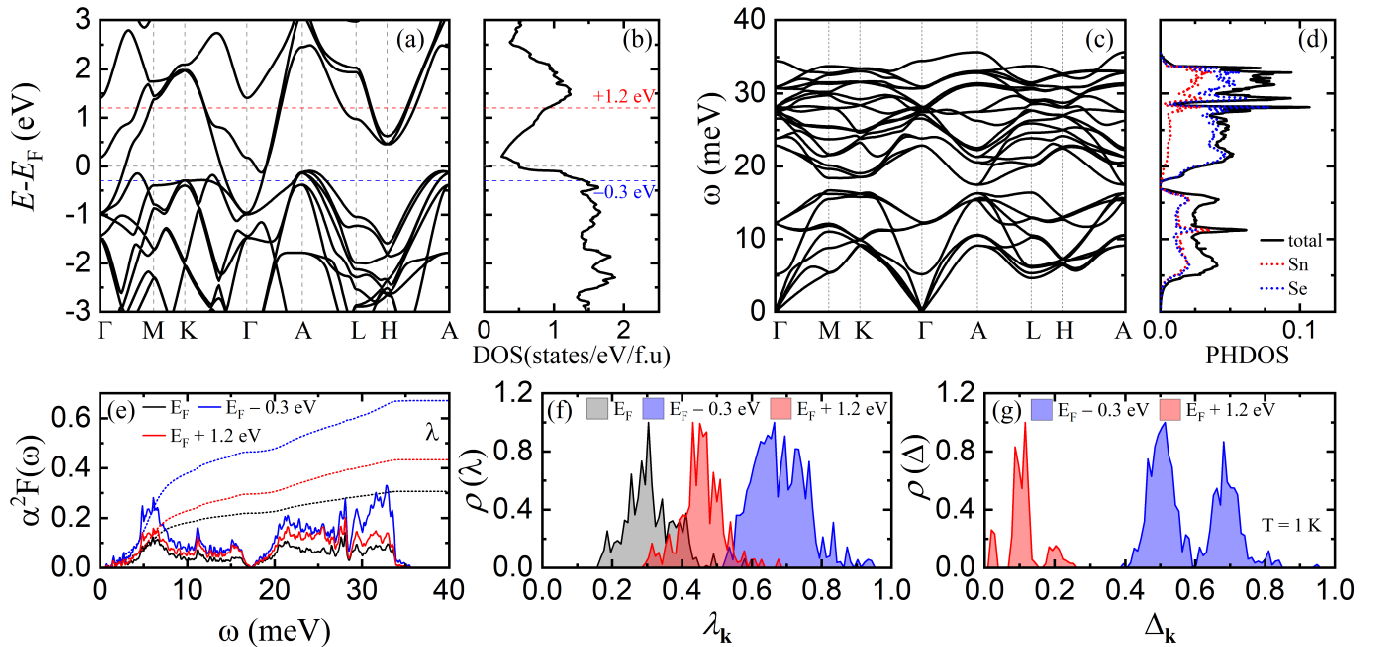


FIG. S21. Calculated (a) band structure, (b) DOS, (c) phonon dispersion, (d) PHDOS, (e) Eliashberg spectral function $\alpha^2 F(\omega)$ and e-ph coupling strength $\lambda(\omega)$, (f) energy distribution of the e-ph coupling strength $\lambda_{\mathbf{k}}$, and (g) energy distribution of the superconducting gap $\Delta_{\mathbf{k}}$ at $T = 1$ K for the $H2-1$ structure in the $\sqrt{3} \times \sqrt{3} \times 1$ supercell of SnSe_2 at 30 GPa. In (e)-(g), black lines show the quantities at the Fermi level, while red and blue lines correspond to the rigid shifts in the Fermi level indicated in (a) and (b). Note that the DOS and PHDOS are plotted per formula unit.

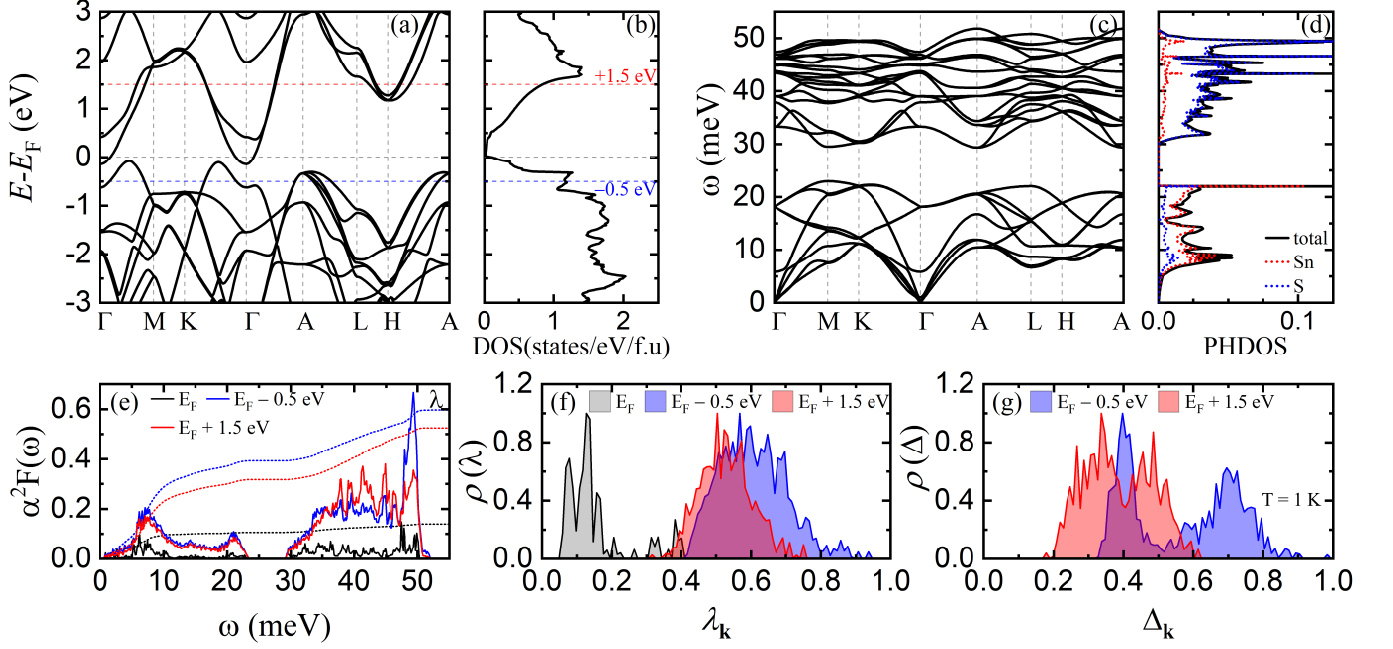


FIG. S22. Calculated (a) band structure, (b) DOS, (c) phonon dispersion, (d) PHDOS, (e) Eliashberg spectral function $\alpha^2 F(\omega)$ and e-ph coupling strength $\lambda(\omega)$, (f) energy distribution of the e-ph coupling strength $\lambda_{\mathbf{k}}$, and (g) energy distribution of the superconducting gap $\Delta_{\mathbf{k}}$ at $T = 1$ K for the $H2-1$ structure in the $\sqrt{3} \times \sqrt{3} \times 1$ supercell of SnS_2 at 30 GPa. In (e)-(g), black lines show the quantities at the Fermi level, while red and blue lines correspond to the rigid shifts in the Fermi level indicated in (a) and (b). Note that the DOS and PHDOS are plotted per formula unit.

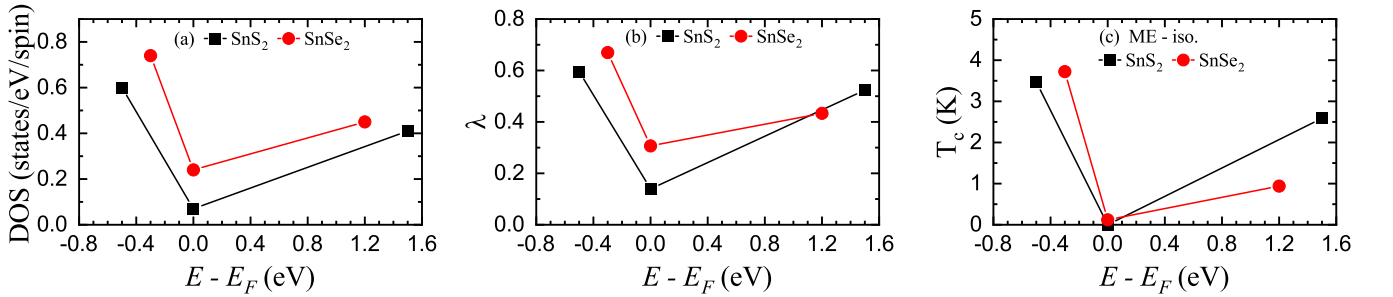


FIG. S23. Variations in (a) DOS at E_F , (b) λ , and (c) T_c as a function of a rigid shift of the Fermi level for the $H2-1$ structure in the $\sqrt{3} \times \sqrt{3} \times 1$ supercell of SnSe_2 (red lines and symbols) and SnS_2 (black lines and symbols) at 30 GPa. In (c), the T_c is obtained from the numerical solutions of the isotropic ME equations.

* rmargine@binghamton.edu

- [1] J. Ying, H. Paudyal, C. Heil, X. J. Chen, V. V. Struzhkin, and E. R. Margine, “Unusual pressure-induced periodic lattice distortion in SnSe₂”, *Phys. Rev. Lett.* **121**, 027003 (2018).
- [2] Y. Zhou, B. Zhang, X. Chen, C. Gu, C. An, Y. Zhou, K. Cai, Y. Yuan, C. Chen, H. Wu, R. Zhang, C. Park, Y. Xiong, X. Zhang, K. Wang, and Z. Yang, “Pressure-induced metallization and robust superconductivity in pristine 1T-SnSe₂”, *Adv. Electron. Mater.* **4**, 1800155 (2018).
- [3] Z. V. Borges, C. M. Poffo, J. C. de Lima, S. M. Souza, D. M. Trichôs, and R. S. de Biasi, “High-pressure angle-dispersive X-ray diffraction study of mechanically alloyed SnSe₂”, *J. Appl. Phys.* **124**, 215901 (2018).
- [4] K. Knorr, L. Ehm, M. Hytha, B. Winkler, and W. Depmeier, “The High pressure behaviour of SnS₂: X-Ray powder diffraction and quantum mechanical calculations up to 10 GPa”, *Phys. Stat. Sol.* **223**, 435 (2001).
- [5] R. M. Hazen, L. W. Finger, “The crystal structures and compressibilities of layer minerals at high pressure. I. SnS₂, berndtite”, *American Mineralogist* **63**, 289 (1978).
- [6] M. Ø. Filsø, E. Eikeland, J. Zhang, S. R. Madsen and B. B. Iversen, “Atomic and electronic structure transformations in SnS₂ at high pressures: a joint single crystal X-ray diffraction and DFT study”, *Dalton Trans.* **45**, 3798 (2016).
- [7] SPGLIB, <https://spglib.github.io/spglib/>.
- [8] S. Hajinazar, A. Thorn, E. D. Sandoval, S. Kharabazde, and A. N. Kolmogorova, “MAISE: Construction of neural network interatomic models and evolutionary structure optimization”, arXiv:2005.12131v2.